Propionyl-CoA carboxylase subunit B modulates PIK3CA-regulated immune-surveillance in a pancreatic cancer mouse model

Han V. Han[1,2], Richard Efem[3], Barbara Rosati[1,3], Sara Maimouni[4], Kevin Lu[4], Ya-Ping Jiang[1], Wei-Xing Zong[4], Richard Z. Lin[1,3]

[1]Department of Physiology and Biophysics, Stony Brook University, Stony Brook, New York

[2]Department of Biomedical Engineering, Stony Brook University, Stony Brook, New York

[3]Northport Veteran Affair Medical Center, Northport, New York, USA

[4]Department of Chemical Biology, Ernest Mario School of Pharmacy, Rutgers-The State University of New Jersey, Piscataway, New Jersey

Corresponding author:

Richard Z. Lin, Stony Brook University, BST 6-180, Stony Brook NY 11790,

631-444-1638, Richard.Lin@stonybrook.edu

Conflict-of-interest Statement

The authors have declared that no conflict of interest exists.

ABSTRACT

Pancreatic ductal adenocarcinomas (PDACs) are resistant to systemic treatments including immunotherapy. Over 90% of PDACs have oncogenic KRAS mutations, and phosphoinositide 3-kinases (PI3Ks) are direct effectors of KRAS. Previously, we demonstrated that genetic ablation of PI3K isoform, *Pik3ca* in the KPC (*Kras*^{G12D}; *Trp53*^{R172H}; *Pdx1-Cre*) pancreatic cancer cell line induced complete tumor elimination by infiltrating T cells in a mouse model. However, clinical trials using PI3K inhibitors for PDAC patients exhibited limited efficacy due to drug resistance. To identify potential contributors to PI3K inhibitor resistance, we conducted an *in vivo* genome-wide gene-deletion screen using the *Pik3ca*$^{-/-}$ KPC (named αKO) cells implanted in the mouse pancreas and discovered propionyl-CoA carboxylase subunit B (PCCB) modulates PIK3CA-mediated immune evasion. Deletion of *Pccb* gene in αKO cells (named p-αKO) allowed tumor progression causing death of host mice even though p-αKO tumors are infiltrated with T cells. Single-cell RNA sequencing revealed that infiltrating clonally expanded T cells in p-αKO tumors were more exhausted as compared to T cells founds in αKO tumors. Blockade of PD-L1/PD1 interaction reversed T cell exhaustion, slowed tumor growth and improved the survival of mice implanted with p-αKO cells. These results indicate that propionyl-CoA carboxylase activity modulates PIK3CA-regulated immune surveillance of PDAC.

INTRODUCTION

Pancreatic ductal adenocarcinoma (PDAC) is one of the most aggressive and lethal cancers, and it is expected to be the 2nd leading cause of cancer death by 2030, with a five-year survival rate of 12% (1). One of the most commonly dysregulated pathways in PDAC is oncogenic KRAS and G12D is the most common KRAS mutation (46%) in PDAC (2,3). Phosphatidylinositol 3-kinases (PI3Ks) are direct effectors of KRAS. There are four PI3K catalytic isoforms and our group have previously shown that PIK3CA isoform plays a critical role in the initiation of PDAC (4) and mediates immune evasion once the tumors are formed (5). Most PDACs are classified as “cold” tumors without infiltrating T cells. To convert PDAC into “hot” tumors, researchers have explored multiple strategies to promote immune responsiveness of PDAC (2,6,7). These approaches encompass targeting immune checkpoint inhibitors, including PD1, CTLA4, LAG3, and TIGIT (8-12), suppressing immunosuppressive cells such as myeloid-derived suppressor cells (MDSCs) and/or tumor-associated macrophages (TAMs) (13-16), enhancing antigen processing and epitope presentation by promoting MHC class I/II cell surface expression (5,17,18) and reinstating the expansion and functionality of dendritic cells (19), targeting key factors implicated in stromal fibrosis to facilitate the infiltration of T cells (20-22), and depleting immunosuppressive signals (cytokines and chemokines) in the tumor microenvironment (TME) that hinder the entry and function of T cells (23-26).

Our group reported that KRAS signaling through PIK3CA can reduce the expression of MHC class I molecules, thus reducing antigen recognition and T cell infiltration (5). We showed that genetic ablation of PIK3CA in KPC (*Kras*^{G12D}*;Trp53*^{R172H}*;Pdx1-Cre*) pancreatic tumor cells led to T cell recognition and complete elimination by the host immune system in a syngeneic orthotopic implantation mouse model (5). This result suggests that targeting PIK3CA may offer a promising approach to enhance the anti-tumor immune response against PDAC.

Several PI3K inhibitors have been FDA approved for treatment of cancers, and alpelisib is the only one approved for specifically targeting the PIK3CA isoform (27). Unfortunately, despite

early promising pre-clinical results, PI3K inhibitors have shown limited efficacy in clinical trials due to drug resistance and dose-limiting adverse effects (28-33). There is a need to identify additional therapeutic targets to overcome the resistance to PIK3CA inhibition. Using the well-characterized syngeneic orthotopic implantation mouse model with the αKO (*Kras*^{G12D}*;Trp53*^{R172H}*;Pdx1-Cre;Pik3ca*$^{-/-}$) cell line, we performed an *in vivo* genome-wide CRISPR gene-deletion screen on the αKO cells and identified propionyl-CoA carboxylase subunit B (PCCB) that could reverse the immune-elimination phenotype. We further discovered that T cells infiltrating the p-αKO (*Kras*^{G12D}*;Trp53*^{R172H}*;Pdx1-Cre;Pik3ca*$^{-/-}$*;Pccb*$^{-/-}$) tumors were suppressed and could not eliminate the tumor cells. However, these exhausted anti-tumor T cells could be reactivated by neutralizing the PD-L1/PD1 axis, restoring the tumor elimination properties of these immune cells.

RESULTS

A Genome-wide CRISPR gene-deletion screen to identify molecules contributing to Pik3ca-mediated pancreatic tumor immune evasion

We previously showed αKO tumors when implanted in immunocompetent mice are recognized by the host immune system, leading to their elimination (5). To identify genes that can reverse this immune recognition phenotype, we performed an *in vivo* genome-wide CRISPR knockout screen in αKO cells. A schema for the CRISPR knockout screen is shown in Figure 1A. Briefly, αKO cells were first infected with the Genome-Scale CRISPR Knockout (GeCKO v2) pooled lentiviral library A, which targets the complete mouse genome of 20,611 genes with three sgRNAs for each gene, as well as four sgRNAs for each of the 1175 miRNAs and 1000 control sgRNAs. Equal portion of the mixed cell pool was implanted into the pancreas of eight immunocompetent C57BL6/J (B6) mice and tumor progression was monitored longitudinally by an IVIS Lumina III *in vivo* imaging system (Figure 1B). When implanted in B6 mice, αKO tumors completely regressed. Therefore, cells with genetically deleted molecules that can reverse the immune recognition phenotype should lead to tumor progression. Indeed, 2 out of 8 mice eight weeks after cell implantation exhibited tumor progression, which were labeled as tumor #1 and tumor #2 (Figure 1B). Tumors were harvested from both mice for further analysis. The remaining mice (6 out 8) exhibited complete tumor regression consistent with the phenotype we previously observed with αKO cells (Figure 1B). Genomic DNA was prepared from both tumors and subjected to next generation sequencing (NGS) to detect the presence of incorporated sgRNA sequences. Sequenced data was analyzed using Model-based Analysis of Genome-wide CRISPR/Cas9 Knockout (MAGeCK), and the counts for each sgRNA sequence are shown in Figure 1C. Somewhat surprisingly, four common sgRNA sequences were identified in both tumors. The four targeted genes are *Pccb* (propionyl-CoA carboxylase), *Nr6a1* (nuclear receptor subfamily 6 group A member 1), *Ldoc1l* (leucine-zipper protein 1), and *Adck3* (aarF-domain-containing kinase 3). Tumor #2 has two additional sgRNA sequences targeting two other genes

that were not present in Tumor #1. Despite the fact that tumor #1 and tumor #2 grew at different rates and were harvested at different time points, week 7 and week 13 respectively, the detected sgRNAs were highly similar, strongly suggesting that the identified genes play critical roles in *Pik3ca*-mediated immune evasion.

In both tumors, *Pccb* sgRNA sequence MGLibA ID 39695 was detected at many orders of magnitude higher than other three sgRNA sequences (Figure 1C). Propionyl-CoA carboxylase (PCC) has two subunits PCCA (propionyl-CoA carboxylase subunit A) and PCCB and catalyzes the carboxylation of propionyl-CoA to methylmalonyl-CoA, which is then converted to succinyl-CoA that enters the tricarboxylic acid cycle (TCA). PCC dysfunction leads to a rare genetic disease called propionic acidemia, which has been extensively studied (34-36). However, PCCB's role in cancer and weather it plays a role in the tumor immune response is completely unknown.

Ablation of PCCB reverses the immune recognition of αKO cells

To validate the genetic screen result, we next genetically ablated *Pccb* in αKO cells using CRISPR/Cas9 techniques and generated the PCCB-null p-αKO cell line. PCCB ablation was confirmed by western blotting (Figure 2A). We next orthotopically implanted p-αKO cells to the pancreas of B6 mice and monitored tumor growth by IVIS imaging (Figure 2B). Most of the mice exhibited tumor formation within one week. In some of the host animals, tumor regressed when they were reimaged at week #2. However, in all of the animals, pancreatic tumors eventually progressed and 9 out of 12 mice died by week #8 when the experiment was stopped (Figure 2B & C). Postmortem examination showed that the three surviving mice had large pancreatic tumors that were also detectable by IVIS imaging (Figure 2B). In comparison, while 100% of mice implanted with KPC cells died by week #3, all mice implanted with αKO cells remained tumor free by week #8 (Figure 2C & D). These results indicate that loss of PCCB can reverse immune recognition of αKO cells.

In vitro characterization of p-αKO cells

In standard 2D culture, p-αKO cells grew at a similar rate compared to αKO cells (Figure 3A). Note that both αKO and p-αKO cell lines exhibited significantly slower growth rate than KPC cells. This reduced growth rate explains, at least in partial, the longer survival time of p-αKO implanted mice compared with KPC-implanted mice, where the median survival of KPC was 15.5 days and the median survival of p-αKO 40.5 days (Figure 2C). Immunoblotting showed no changes in phosphorylation of PIK3CA's downstream effector AKT at both Thr308 and Ser473 residues. As expected, phosphorylation of PRAS40, which is a direct effector of AKT, was also downregulated in both cell lines lacking PIK3CA as compared to KPC cells. PTEN is a negative regulator of the PI3K-AKT pathway, and its expression was not different between the three cell lines (Figure 3B). In summary, the loss of PCCB did not reverse the changes in PIK3CA-AKT signaling in αKO cells. These results indicate that progression of p-αKO tumors is through a pathway independent of PI3K and AKT.

Since PCCB encodes a mitochondrial enzyme, the mitochondrial function of KPC, αKO, and p-αKO cell lines was evaluated by measuring the oxygen consumption rate (OCR) with Seahorse XF Cell Mito Stress Test kit (Figure 3C). Oligomycin is an ATP synthase inhibitor that suppresses mitochondria ATP production and shifts the energy production to glycolysis. When oligomycin was added, similar levels of OCR reductions were observed in all three cell lines. The next addition of carbonyl cyanide-4 (trifluoromethoxy) phenylhydrazone (FCCP) induced oxygen consumption and the final addition of a mixture of rotenone and antimycin A shuts off the mitochondrial respiration, all induced similar changes in the three cell lines (Figure 3C). We next performed an untargeted liquid chromatography-mass spectrometry (LC/MS) measuring the intracellular metabolites of αKO vs. p-αKO cells. We found comparable levels of metabolites in the TCA and glycolytic pathways (Figure 3D). Taken together, the metabolic measurements

indicate that increased growth of p-αKO cells *in vivo* is probably not due to PCCB-related mitochondrial metabolic changes.

T cells infiltrate p-αKO tumors

Our previous study demonstrated that regression of αKO tumors is due to T cell infiltration and subsequent elimination by the host immune system (5). We performed immunohistochemistry (IHC) to assess the status of infiltrating T cells in p-αKO, αKO, and KPC tumors. After implantation, IVIS imaging was used to confirm presence of tumors, which were then harvested for analysis. H&E staining confirmed tumor formation (Figure 4A) and immediate adjacent tissue sections were stained for infiltrating T cells using anti-CD3, CD4 and CD8 antibodies. Unexpectedly, p-αKO tumors were also highly infiltrated with T cells, similar to αKO tumors, and as expected, KPC tumors were mostly devoid of T cells (Figure 4A & B). Therefore, the conversion of cold KPC tumor into inflamed αKO tumor upon genetic deletion of *Pik3ca* in KPC was not reversed by ablation of PCCB.

Increased expression of immune checkpoints in p-αKO tumors

As high expression of checkpoint inhibitory receptors is associated with reduced ability to perform cytotoxic functions, we examined whether T cell checkpoint inhibitory receptors, including programmed cell death 1 (PD-1), cytotoxic T-lymphocyte associated protein 4 (CTLA-4), T cell immunoreceptor with Ig and ITIM domains (TIGIT), lymphocyte activating 3 (LAG3), and hepatitis A virus cellular receptor 2 (TIM3) were altered upon PCCB ablation. Tumor tissues harvested from αKO and p-αKO implanted mice were stained by IHC with a panel of checkpoint marker antibodies (Figure 5A). Compared with αKO tumor sections, PD1, CTLA4 and LAG3 exhibited significant increases in expression levels in p-αKO tumors, whereas TIGIT and TIM3 showed similar expression levels (Figure 5B). These results suggest that infiltrating T cells in p-αKO tumors might be exhausted with compromised anti-tumor cytotoxic activity.

T cells infiltrating p-αKO tumors have gene expression profiles consistent with an "exhausted" phenotype

To further investigate the status of infiltrating T cells in αKO and p-αKO tumors, single cell RNA sequencing (scRNA-seq) was conducted in combination with concurrent T cell receptor (TCR) repertoire sequencing. On day #12 post implantation in B6 mice, αKO and p-αKO tumors were harvested and dissociated to generate single cell suspensions. $CD4^+$ and $CD8^+$ T cells were isolated using microbead preparations. Both the transcriptional expression and TCR repertoire profiles were obtained using 10x genomic protocols (Figure 6A). After strict quality control filters as described in Methods, a total of 11209 cells were captured and pooled to generate unsupervised clustering by applying principal component analysis (PCA) using the Seurat software. The clustering was then visualized by the uniform manifold approximation and projection (UMAP), which showed that the cells were classified into 9 unsupervised groups solely based on their gene expression profiles (Figure 6B). Cell type annotations were decided by ProjectTILs, a computational method that annotates cell types by projecting scRNA-seq data into reference profiles built from previously published characteristic canonical cell markers (37). The 9 clusters are annotated as naïve-like Cd4 T cells (Cd4_NaiveLike), early activated Cd8 T cells (Cd8_EarlyActiv), effector memory Cd8 T cells (Cd8_EffectorMem), naïve-like Cd8 T cells (Cd8_NaiveLike), exhausted Cd8 T cells (Cd8_Tex), precursor exhausted Cd8 T cells (Cd8_Tpex), follicular helper T cells (Tfh), Cd4 helper type 1 cells (Th1), and regulatory T cells (Treg).

Among the identified 9 groups, Cd8_EffectorMem, Cd8_Tex, Cd8_Tpex, Tfh, Th1, and Treg displayed notable differences between αKO and p-αKO tumor-infiltrating T cells (Figure 6B). In comparison to the αKO tumor, the percentages of exhausted T cells (Cd8_Tex and, Cd8_Tpex), and immunosuppressive Tregs as well as Tfh were notably elevated in the p-αKO tumor. In contrast, there are higher percentages of Cd8_EffectorMem and Th1 cells in the αKO tumor.

Other groups, such as Cd4_NaiveLike, Cd8_NaiveLike, and Cd8_EarlyActiv, showed relatively similar levels between αKO and p-αKO tumors. These results support the hypothesis that p-αKO tumors exhibit an immunosuppressive microenvironment that can inactivate anti-tumor cytotoxic T cells. As expected, the αKO tumor was mostly infiltrated with Cd8_EffectorMem and Th1 cells, both of which promote tumor cell killing. mRNA levels of Pdcd1, Ctla4, Lag3, Tigit, and Tim3 for $Cd8^+$ T cells also revealed that T cells in p-αKO tumors have a relatively higher immune checkpoint markers compared with αKO tumors (Figure 6C). We next calculated T exhaustion scores using SignatuR, a single-cell RNAseq analysis package in the R software. Based on the average expression levels of the 5 T cells checkpoint inhibitory receptors—Pdcd1, Ctla4, Lag3, Tigit, and Tim3—for each T cell in each subgroup. The exhaustion scores are notably higher for T cells in p-αKO tumor than in αKO tumor in every group, even in the Cd8_EffectorMem group (Figure 6D).

Recognition of tumor antigens should lead to expansion of T cell clonotypes. TCR repertoire analysis was performed on sequences with both α and β chains of TCR and with a mapped gene expression sequence. Adaptive immune responses rely heavily on the diverse expressions of TCR repertories. Sequencing the TCR repertoire thus can identify clonotypic diversity and clonal selection and expansion (38). A clonotype is defined as 3 or more cells with identical TCR sequences. A clonal size of 3 to 50 is defined as small expansion, and clonal size of over 50 is defined as large expansion. By TCR analysis, we found extensive T cell clonotype expansion in both tumor types. As expected, we identified numerous (1894) TCR clonotype in the αKO tumor. Interestingly, we found even more clonotypes (2315) in the p-αKO tumor. The clonal size distribution for $CD4^+$ and $CD8^+$ ranges from the smallest clone, which was 1 cell, to the most numerous $CD8^+$ clonotype in the αKO tumor has 180 cells whereas the most numerous $CD8^+$ clonotype has 676 cells (Figure 7A). Both tumor types contained a few dominant clonotypes with large numbers of cells. Figure 7B lists the large expansions with clonal size of over 50 for $CD4^+$ and $CD8^+$ clonotype in both tumors. In summary, these results

indicate expansion of T cell clonotypes that are potentially cytotoxic against tumor cells are present in both tumor types.

We next mapped the TCR profiling datasets to the single-cell gene expression datasets and then color coded by the size of each clonotype (Figure 7B). Clone sizes of less than 3 were mainly found in the naïve $CD4^+$ and $CD8^+$ T cell groups, suggesting that these were non-tumor reactive T cells. The remaining cells were deemed to have expanded in response to tumor antigens and are thus tumor reactive T cells. These cells were divided into small (3-50) and large clonal expansion groups (≥51). Among $CD8^+$ T cells, 54.6% of TCRs in αKO tumor were clonal, i.e., greater than 3, and 69.1% of TCRs the in p-αKO tumor were clonal. Within $CD4^+$ T cells, 51.5% of TCRs in αKO tumor were clonal and 43.7% of TCRs in the p-αKO tumor were clonal. For T cell clones in αKO tumor, regardless of the clonal size, CD8 clones largely mapped to the Cd8_EffectorMem group and $CD4^+$ clones predominantly fell within the Th1 group, both exhibited a highly heterogeneous composition. For the p-αKO tumor, other than the highly heterogeneous composition with varying degrees of clonal expansions in both Cd8_EffectorMem and Th1 groups, large expansions mapped to the Cd8_EffectorMem, Cd8_Tex, and Treg groups (Figure 7C & D). This observation suggests that in the αKO tumor, T cells sharing similar gene expressions recognized different tumor antigens and expanded in response to generate a functional immune response and formed different clones of Cd8 effector memory T and Th1 cells. In the p-αKO tumor, most clonal expansions mapped to either Cd8_Tex or Treg, which are consistent with the immune non-reactive phenotype, some expanded clones are mapped to Cd8_EffectorMem, which should have anti-tumor effects (Figure 7D). However, exhaustion scores of the Cd8_EffectorMem group in the p-αKO tumor showed a relatively higher exhaustion profile than the Cd8_EffectorMem T cells in the αKO tumor (Figure 7E). Collectively, these results showing the p-αKO tumor is mostly infiltrated with exhausted $CD8^+$ T cells and $CD4^+$ Tregs. This may explain why the loss of PCCB can reverse the αKO immune elimination phenotype, leading to tumor progression (Figure 2C).

Inhibition of PD1/PD-L1 checkpoint leads to elimination of most p-αKO tumors

To investigate whether blocking the PD1/PD-L1 immune checkpoint would reactivate the exhausted anti-tumor T cells, we implanted p-αKO cells into a PD1-null mouse line bred in the B6 genetic background (Figure 8A). After 8 weeks when the experiment ended, 8 out 9 mice were still alive and 5 of the animals were tumor free (Figure 8B & C). To test if pharmacological blockade of PD1/PD-L1 will achieve a similar result, we implanted p-αKO cells in wild-type B6 mice and then treated them weekly with a neutralizing anti-PD antibody or vehicle control (Figure 8A). After 8 weeks of treatment, 9 out 13 anti-PD1-treated mice were alive whereas only 2 out 9 vehicle-treated mice survived (Figure 8B). Four mice in the anti-PD1-treated group remained tumor free. In contrast, all vehicle-treated mice developed large pancreatic tumors even the two surviving mice at week #8 (Figure 8C).

To confirm that PD1/PD-L1 blockade reactivated anti-tumor T cells, we performed scRNA-seq on T cells isolated from p-αKO tumors implanted in wild-type and PD1-null mice. As a control, we also perform the same analysis on an αKO tumor implanted in wildtype mice. Clonal size distribution indicated that large clonal expansions were observed in all four groups (Figure 9A). In one of two PD1-null tumors analyzed, the highly expanded $CD8^+$ T cell clones infiltrating the p-αKO tumor implanted in PD1-null mice exhibited an activated gene expression profile (Figure 9B). In contrast, the other p-αKO tumor implanted in PD1-null mice showed multiple highly expanded T cell clones that have exhausted gene expression profiles (Figure 9B). This may explain why PD1/PD-L1 blockade was only partially effective and thus resulted in tumor progression and death of some host mice (Figure 8B). As expected, the expanded $CD8^+$ T cell clones found in p-αKO tumor implanted in wild-type mice again exhibited exhausted gene expression profiles, and αKO tumor implanted in wildtype mice again was found with highly expanded cytotoxic T cell clones that likely eliminated the pancreatic tumor cells (Figure 9B &

C). In summary, these results indicate that regression of p-αKO tumors in mice following PD1/PD-L1 blockade is due to reactivation of anti-tumor cytotoxic T cells.

PCCB expression in human pancreatic cancer

To explore the potential significance of *PCCB* expression in PDAC patients, we queried the Cancer Genome Altas Program (TCGA) database and compared the overall survival of patients with high *PCCB/PIK3CA* ratio to patients with low *PCCB/PIK3CA* ratio. Compared with patients with lower *PCCB/PIK3CA* ratio, patients with higher ratio trended to have better survival (Figure 10A). Additional clinical data of PDAC patients were obtained from gene expression omnibus (GEO) database. The GSE15471 is an expression analysis of 36 PDAC patients from the Clinical Institute Funding, where tumors and matching normal pancreatic tissue samples were obtained at the time of surgery. The GSE16515 is the expression data from Mayo Clinic, and it consists of 36 tumor samples and 16 normal samples. Both data revealed significantly lower *PCCB* expressions in tumor sections compared with adjacent normal tissues (Figure 10B), which is consistent with our observation that low *PCCB* levels lead to tumor progression.

DISCUSSION

The PI3K signaling pathway plays an important role in regulating the immune microenvironment in PDAC, and several PIK3CA inhibitors have shown potential in converting immune-deficient cold tumors into hot tumors (39-44). In our previous study utilizing a PDAC mouse model, we observed that downregulation of PIK3CA in tumor cells can lead to their recognition and elimination by the immune system (5). In the current study, we conducted a genome-wide *in vivo* CRISPR screen to discover potential molecules that can confer resistance to PIK3CA inhibition. We found that loss of PCCB, a subunit of the mitochondrial enzyme propionyl-CoA carboxylase, can completely reverse the immune recognition phenotype caused by the downregulation of PIK3CA. Ablation of PCCB in pancreatic tumor cells lacking PIK3CA leads to immune evasion, tumor progression, and death of the host animal. Furthermore, this immunological effect is reversed by blocking the PD-L1/PD1 axis, leading to T cell elimination of p-αKO (PCCB/PIK3CA double-null) tumor cells. Our single-cell sequencing results indicate that loss of PCCB in tumor cells leads to exhaustion of expanded clonal cytotoxic T cells targeting the tumor and blocking the PD-L1/PD1 interaction reactivates the clonal anti-tumor T cells.

While loss of PCCB in αKO resulted in tumor progression, these tumors retain the inflamed phenotype characterized by T cell infiltration in the tumor microenvironment (TME). IHC staining demonstrated a potent increase in the levels of checkpoint inhibitory markers in p-αKO tumor sections consistent with a T cell exhaustion phenotype. Employing scRNA-seq analysis, we analyzed the T cells infiltrating both αKO and in p-αKO tumors, uncovering that PCCB ablation led to the expansion of exhausted CD8 T cells, particularly $Pd1^{+}$ CD8 T cells. Notably, when p-αKO cells were implanted in $PD1^{-/-}$ mice, a robust improvement in mice survival was observed at the end of the experiment, suggesting that the immune evasion in p-αKO tumors is partially attributable to elevated PD1 expression on T cells. Treatment the p-αKO tumors with an anti-PD1 neutralizing antibody yielded similar results, highlighting the potential therapeutic application of anti-PD1 antibody for PDAC treatment in combination with a PIK3CA inhibitor.

Recent research has emphasized the potential of combination therapy involving both PI3K and PD1 inhibitors in cancer treatment. For instance, Isoyama et al. (2020) reported improved antitumor effects in melanoma and fibrosarcoma models when combining PI3K inhibitors with PD-1 blockade. This combination therapy decreased Tregs and increased tumor specific $CD8^+$ T cells, leading to enhanced antitumor activity (45). Similarly, Collins et al. (2021) conducted an in vivo expression screen with a pool of known oncogenes and identified oncogenes that promote resistance to anti-PD1 treatment in a colon carcinoma model. They found that the expression of PIK3CA confers resistance to immunotherapy, which can be reversed by treatment with a PI3K inhibitor. These results provide further support for the potential benefits of combining PI3K inhibitors with PD1 blockade for cancer treatment (46). Future studies can test this drug combination using our orthotopic implantation model and in genetically modified mouse models that develop spontaneous PDAC.

Although the administration of anti-PD1 neutralizing antibody showed promising results, the treatment alone is 100% effective. Indeed, our scRNA-seq result from one of the PD1-null mice showed that not all exhausted T cells were reactivated, which may explain why some of the mice still succumb to tumor progression despite PD-L1-/PD1 blockade. Future studies with concurrent blockade of other immune checkpoints such as TIGIT, LAG3, CTLA4 or TIM3, with anti-PD1 may be very informative.

While our findings highlight the involvement of PCCB in resistance to PI3K inhibition through the upregulation of PD1 expression on T cells, the precise underlying mechanism remains unclear. Previous studies primarily focused on the role of *Pccb* in the genetic disease propionic acidemia (PA), caused by mutations in *Pccb* or *Pcca* subunits, which impair PCC function (34). Dysfunctional PCC leads to the accumulation of propionyl CoA and other byproducts such as propionylcarnitine (C3), methylcitrate (MC), and 3-hydroxypropionate (3OHPA) (47,48). Intracellular metabolite analysis by LC-MS showed elevated MC and C3 levels upon *Pccb* deletion, although the enrichment did not reach statistically significant levels (supplementary

figure 1). Importantly, intracellular propionyl-CoA levels were similar between αKO and p-αKO cells, potentially due to its conversion to MC and C3. However, the accuracy of propionyl-CoA detection is challenging due to its relatively small quantity.

Although a direct relationship between PCCB and the immune response has not been reported, several papers reported the anti-inflammatory properties of propionate, a byproduct of dysfunctional PCC. Smith et al. (2013) reported that propionic acid regulates colonic Treg (cTreg) homeostasis in the gut lumen. Propionic acid supplementation in the drinking water of germ-free (GF) mice increased cTreg frequency and number in the gut lumen, while Tregs in the spleen, mesenteric lymph nodes, and thymus remained unaffected. Treatment of cTregs isolated from GF mice with propionate led to increased Foxp3 and IL10 expressions, both of which play important roles in Treg-mediated immune suppression. Additionally, cTregs exhibited a higher proliferation rate when co-cultured with propionate (49). Another study by Tedelind et al. (2007) reported that propionate suppressed the secretion of TNFα and IL8 from neutrophils and inhibited the NF-kB pathway and expression of immune-related genes in a colon cell line (50). Hogh et al. recently reported that propionate upregulated the surface expression of the immune stimulatory NKG2D ligands MHC-class-I-related family (MICA/B) on several cancer cells and activated T cells, mediated by mTORC2 (51). These indirect observations suggest a link between *Pccb* and immune responses, although the findings are somewhat conflicting. Furthermore, cytokines and other mechanisms within the TME might be involved in the upregulation of PD1 expression on T cells in p-αKO tumors. Moreover, comparing cells grown *in vitro* to tumor growth *in vivo* is challenging due to the complexity of the TME and potential crosstalk between immune cells and metabolism system. Therefore, future studies should conduct RNAseq analysis of *in vivo* tumor cells surviving within the TME to uncover the *in vivo* mechanisms of immune evasion upon *Pccb* knockout.

To improve survival rates, it is crucial to incorporate other immunotherapies targeting additional checkpoint inhibitory receptors, such as CTLA4, LAG3, and TIGIT. While anti-CTLA4

and anti-PD1 are standard treatments for many solid tumors, TIGIT and LAG3 have emerged as promising new targets for cancer immunotherapy. LAG3, although demonstrating limited efficacy as a monotherapy, is frequently used in combination with other checkpoint inhibitors (12). Similarly, while anti-TIGIT antibodies have shown remarkable effectiveness in treating solid tumors, the dual blockade of PD-1 and TIGIT has demonstrated superior clinical benefits in cancer treatment (52-54). Notably, our IHC data revealed significant upregulation of both TIGIT and LAG3 in p-αKO tumors, suggesting that employing additional immune checkpoint inhibitors in combination with PD1 inhibition may further enhance survival outcomes.

Our study is the first to report an association between PCCB and PIK3CA. We utilized PIK3CA knockout cells (αKO) instead of conventional PIK3CA inhibitors to avoid off-target effects reported in previous studies (55-58), providing a more specific and accurate assessment of the role of PIK3CA in regulating immune responses in PDAC. We employed an orthotopic mouse model for our CRISPR screen, which more closely mimics the tumor microenvironment of human PDAC. Our genome-wide screen study identified PCCB as a key regulator of resistance to PI3K inhibition. We showed that PCCB regulates immune evasion by promoting increased PD-L1 expression in anti-tumor cytotoxic T cells. Therefore, our findings suggest that PDAC resistance to PI3K inhibitors and checkpoint inhibitors might be overcome by using the two drugs in combination. Future pre-clinical and clinical studies can directly test these FDA-approved drugs and perhaps in combination with other treatment modalities for this deadly cancer.

METHODS

Cell Culture and Reagents. KPC, αKO, and p-αKO were all cultured in complete DMEM media (Gibco, Thermo Fisher Scientific) with 10% FBS (Corning 35-015-CV) and 1% P/S (penicillin/streptomycin: Gibco 15140-122), incubated at 37 °C with 5% CO2. The KPC cell line was a gift from Dr. David Tuveson (Cold Spring Harbor) and was confirmed to possess a G-to-D mutation in the KRAS gene (KRASG12D) and a silent mutation in the transformation related protein 53 gene (TP53R172H) by mutation analysis in a previous study (5). The preparation of KPC and αKO cell lines were descripted before (5). Briefly, KPC cells were infected with lentiviral particles containing CMV-firefly luciferase with a neomycin selection marker (Cellomics Technology, PLV-10064). After 48-hour transfection, KPC cells were selected with 1.5 mg/ml G418, and the luciferase expression was confirmed by the IVIS Lumina III imaging system (Xenogen). KPC cells that express luciferase signals are referred to as WT KPC. *Pik3ca*$^{-/-}$ (αKO) KPC cell lines were generated by transfecting WT KPC cells with *Pik3ca* CRISPR/Cas9 αKO and HDR plasmids (Santa Cruz Biotechnology, sc-422231 and sc-422231-HDR). Transfected cells were selected with 5 mg/mL puromycin and sorted based on red fluorescent protein (RFP) by fluorescence-activated cell sorting (FACS) on a FACSAria (BD Biosciences). RFP^{+} cells were serially diluted in a 96-well plate to generate single cell clones, and clones that showed an absence of PIK3CA protein on western blot were retained (referred to as αKO cell lines). In order to knock out *Pccb* from αKO cell lines, αKO was transfected with *Pccb* CRISPR/Cas9 KO plasmid (Santa Cruz Biotechnology, sc-42658) and incubated for 48 hours. Again, western blot was used to verify PCCB expression and cells without the presence of PCCB and PIK3CA are referred to as p-αKO cell lines.

GeCKO v2 Lentiviral Library Preparation and Infection. The mouse GeCKO v2 library was obtained from Addgene (#1000000052). LentiCRISPRv2 is a one-vector plasmid system for the mouse GeCKO (Genome-scale CRISPR Knockout) pooled library. The sublibrary A contains

67,405 sgRNAs targeting 20,611 protein-coding genes, 1175 microRNAs and 1000 control sgRNAs. To ensure no loss of representation, the GeCKO library A was amplified by first electroporating the library to Endura ElectroCompetent cells and then transforming to LB agar plates. The colonies from the LB agar plates were harvested and purified by Maxiprep. To produce lentivirus, the plasmid was used to transfect HEK293FT cells by lipofectamine 2000 plus reagent with packaging plasmids pVSVg and psPAX2. After incubating for 2 days, the lentiviral supernatant from the HEK293FT cells were pooled and filtered to get rid of cellular debris. Then the lentiviral titer was determined through transduction. To calculate the MOI and optimal kill curve, cells were treated with a serial dilution of concentrated virus followed by puromycin selections the next day with titrations of 0, 0.5 mg/ml, 1 mg/ml, and 2 mg/ml. After 48 hours of treatment, cell apoptosis was measured with PI and Hoechst staining to determine the concentrations of viral titer and puromycin that give approximately an MOI of 0.2-0.4 with nearly 100% killing (1:10 dilution). To ensure 350x of library coverage, 1x 10^7 αKO cells were seeded, and infected with 1:10 dilutions of the viral titer aiming for a MOI of 0.2-0.4.

CRISPR Knockout Screen in an Orthotopic Pancreatic Implantation Mouse Model. After incubating the transduced αKO cells for 2 days, 7.5×10^5 of the transfected cells in 30ml of PBS were prepared for each mouse and were implanted in the pancreas of 9 immunocompetent wild-type C57BL/6J mice (B6; Stock#000664). To monitor tumor progression, 100 mg/kg RediJect D-Luciferin (PerkinElmer 770504) was injected intraperitoneally into mice followed by imaging on the IVIS Lumina III imaging system (Xenogen) to monitor tumor progression. Data were analyzed using Living Image v4.3.1 software.

Orthotopic Pancreatic Implantation Mouse Model. All the C57BL/6J mice (#000664) and PD-$1^{-/-}$ mice (#028276) were purchased from Jackson Laboratories. The orthotopic implantation surgeries have been described previously (5). Briefly, cells were trypsinized and washed twice

with PBS, then counted with a cell counter to prepare $5x10^5$ cells in 30 µl of PBS per mouse for injection (or 7.5 $x10^5$ cells for the screen). Mice were anesthetized with a combination of 100 mg/kg ketamine and 10mg/kg xylazine, followed by a small vertical incision made over the left lateral abdominal area. The pancreas was then located with the aid of a light microscope, and the injection was made at the head of pancreas by a sterile Hamilton syringe with a 27-gauge needle. After sutures, mice were given an intraperitoneal injection of 2 mg/kg ketorolac.

Mouse Survival Studies. Mice implanted with tumor cells (KPC, GeCKO treated αKO, αKO cells, and p-αKO cells) were monitored by IVIS imaging weekly. Mice with weight loss > 15% body weight and/or inability to move were euthanized as these were considered the endpoint. For mice implanted with p-αKO cells, week 8 was set as the endpoint of the experiment and any surviving animals were euthanized.

Single Cell Suspension. Pancreas with tumor tissues were harvested from mice on day 12 after tumor implantation. After excluding lymph nodes, tissues were washed with cold PBS and minced with scissors in the hood. The minced tissues were washed with PBS, then digested in 5 ml of 1mg/ml Collagenase type V (Worthington LS005282) solution dissolved in HBSS for 20 minutes at 37 °C. 2ml of Roche Red Blood Cell Lysis Buffer (Millipore Sigma 11814389001) was used per sample to get rid of red blood cells, then passed through 40µm cell strainer to generate single cells.

Enrichment of $CD4^+$ and $CD8^+$ T Cells from Dissociated Pancreatic Tumors. 10µl of CD4 (TIL) MicroBeads (Miltenyi Biotec 130-116-475) and 10µl of CD8 (TIL) MicroBeads (Miltenyi Biotec 130-116-478) were added to 90µl of single cell suspensions (up to 10 million cells each) and incubated at 4 °C for 15 minutes. After adding the depletion wash buffer to a final volume of 500µl for up to 50 million cells, the mixture was separated in a LS column (Miltenyi Biotec 130-

042-401) by the magnetic field of the MACS Quadro separator. The flow-throughs were CD4 and CD8 negative cells, and the magnetically labeled cells that were flushed out after removing the magnetic field were CD4 or CD8 positive T cells. The isolated cells were centrifuged at 300xg 4°C for 5 minutes and resuspended in PBS with 0.1% of BSA to generate $1e^6$/ml of cells.

scRNAseq Library Preparation with 10x Genomics Platform. Following the manufacturer's protocol, single cell 5' library were prepared from the enriched cell suspension. Briefly, after diluting the single cell suspension to approximately $0.7\text{-}1.2e^6$/ml, they were combined with reverse transcription (RT) reagents, Gel Beads containing barcoded oligonucleotides, and oil on a microfluidic chip to form reaction vesicles called Gel Beads in emulsion (GEMs). Within each GEM, a single cell was lysed and reverse transcripted to cDNA, followed by PCR amplification of cDNAs. Single cell RNA sequencing library was then prepared using the Chromium Next GEM Single Cell 5' Kit v2 (PN-1000265) and the Chromium Single Cell Mouse TCR Amplification kit (PN-1000254).

Next-generation Sequencing and Data Analysis. Genomic DNA was extracted both from the primary tumor and metastatic sites to perform next generation sequencing in order to identify enriched sgRNAs. Qiagen DNeasy Blood & Tissue Kit (#13323) was used to extract DNA according to the manufacturer's protocol. The concentration of DNA was determined by NanoDrop ND 1000. NGS libraries were prepared by a two-step PCR described before (59,60). All PCR reactions were performed with Herculase II Fusion DNA Polymerase (Agilent K3467). The first PCR (PCR1) utilized primers specific to the sgRNA-expression vector to amplify the sgRNA containing region, in order to preserve full complexity of the GeCKO library. To achieve a 350-fold coverage of the sgRNA library, approximately 200 mg of gDNA for each sample was used, and thus approximate 67 PCR1 reactions were performed for each sample (3 µg gDNA/50 µl reaction). The second PCR (PCR2) is performed to add barcoded adaptors—P7

and P5—to the products from the first PCR, so it allows multiplex sequencing on Illumina NextSeq. For our 67,405 mGeCKOa sgRNA library, at least 7 PCR2 reactions were performed (one 100 µl reaction per 10^4 constructs in the library). Before sequencing, DNA quality and quantity were determined by Qubit dsDNA BR Assay Kit and Agilent 2200 TapeStation Analysis. All samples were sequenced on Illumina NextSeq 550 sequencer. The sequencing data was processed for sgRNA representation. The 8bp barcodes were first demultiplexed from the sequencing reads, followed by adapter trimming. The remaining spacer sequences were aligned to the designed sgRNA library by bowtie, with tolerance of a single nucleotide mismatch. The number of mapped sequences were imported into R/RStudio to quantify the total number of reads. Besides, the computational tool MAGeCK (model-based analysis of genome-wide CRISPR-Cas9 knockout) was used to confirm the identified mapping counts.

scRNAseq Data Analysis. The Cell Ranger v7.0.0 pipeline was used to demultiplex and align sequencing data to the “ENSEMBL GRCm39” mouse transcriptome to generate gene expression matrices. The Cell Ranger VDJ pipeline was used to assemble sequences and identify paired clonotypes on the V(D)J libraries. The gene expression matrices were further analyzed by the Seurat R package. Three quality control criteria were employed to filter the matrices to exclude unwanted sources of variations: number of detected transcripts, genes, and percent of reads mapping to mitochondrial genes. Cells with UMIs over the interquartile range of 95% (potential doublets) and under 1000 (potential fragments) or a mitochondrial proportion higher than 20% (potential apoptotic) were removed. Moreover, we used the Doublet Finder R algorithm to further eliminate doublet contamination. After the quality control, we annotated cellular identity using the R package SingleR, which assigns each cell to a reference type that has the most similar expression profile with. In further analysis, sctransform package in Seurat was used to normalize UMI count data. The principal component analysis (PCA) of high-dimensional data was performed to identify highly variable genes in each sample, and the top

principal components were selected for unsupervised clustering of cells with a graph-based clustering and visualized with Uniform Manifold Approximation and Projection (UMAP).

Western Blotting. Cells were washed twice by PBS followed by lysis in RIPA buffer (50 mM HEPES, pH 7.4, 10 mM sodium pyrophosphate, 50 mM NaF, 5 mM EDTA, 1 mM sodium orthovanadate, 0.25% sodium deoxycholate, 1% NP40, 1 mM PMSF, and protease inhibitor cocktail (Sigma P8340). After centrifuge, cell lysates were collected, and proteins were separated by SDS-PAGE gel followed by semi-dry transfer onto nitrocellulose membranes. After blocking with 5% milk in tris-buffered saline plus 0.1% Tween 20 (TBST), primary antibodies prepared in a 1:1000 dilution with TBST for overnight. After incubating the membrane with horseradish peroxidase (HRP) linked secondary antibodies (Thermo Fisher Scientific #62-6520 & #31460) in a 1:5000 dilution with TBST, signals were developed by adding ECL reagent or SuperSignal West Femto (Thermo Scientific 34095). Signals were detected by a FluorChem E imager (ProteinSimple). Primary antibodies used: PCCB: Millipore sigma HPA036939; PIK3CA: Cell Signaling #4249S; HSP90: Cell Signaling #4874S; PTEN: Cell Signaling #9559S; pAKT (Thr308): Cell Signaling #9275S; pAKT (Ser473): Cell Signaling #4051S; AKT 1/2/3: Santa Cruz Biotechnology sc-377556; actin: Millipore Sigma #A2103; PPRAS40: Cell Signaling #2997S.

Cell Proliferation Assay. 2500 cells were plated in triplicates for each cell line on a 12-well plate on day 0. From day 1 to day 4, cells were washed with PBS, trypsinized and resuspended with completed media and then stained with trypan blue (Invitrogen T10282) with a 1:1 dilution. The cells were then counted using Countess II automated cell counter (Life Technologies). Cell numbers were plotted by GraphPad Prism 9.

Real-time Metabolic Analysis. The Seahorse XF96 extracellular flux analyzer (Seahorse Bioscience, USA) was utilized to measure the oxygen consumption rate (OCR). Cells were

cultured in 96-well XF microplates with 20,000 cells per well and incubated for 18 hours at 37°C. To evaluate mitochondrial activity, sequential injections of oligomycin, the electron transport chain uncoupler FCCP, and specific inhibitor of the mitochondrial respiratory chain were performed. The OCR data were normalized to cell number.

LC-MS. To assess the total metabolite levels, cells were plated in 6-well plates in triplicates with equal cell numbers for each well. After cells were washed three times with PBS, a mixture of methanol, acetonitrile, and water with formic acid was quickly added to the dishes. The plates were then placed on ice for 5 minutes, followed by the addition of 15% NH_4HCO_3 to neutralize the acetic acid. The cells were collected by scraping the centrifuged, and the resulting supernatant was used for LC-MS analysis. The LC-MS employed hydrophilic interaction chromatography (HILIC) coupled with electrospray ionization to a Q Exactive PLUS hybrid quadrupole orbitrap mass spectrometer (Thermo Scientific). A specific LC separation was carried out using an XBridge BEH Amide column, with a gradient of solvent A and solvent B. The gradient varied over a specific time frame, and the flow rate, injection volume, and column temperature were controlled. The metabolite features were extracted using MAVEN software, considering the labeled isotope and a mass accuracy window. The isotope natural abundance and tracer isotopic impurity were corrected using AccuCor. The LC-MS and data analysis was done by Metabolomics Shared Resource at the Rutgers Cancer Institute of New Jersey.

Histology. Mouse tumors were fixed in 10% formalin for 24 hours. Tissue processing was done by Leica ASP300S Tissue Processor. After embedding with paraffin, tissues were sectioned into 4μm sections. H&E staining was performed using Hematoxylin and eosin. Immunohistochemistry (IHC) was performed by deparaffinization and rehydration of the tissue sections, followed by antigen retrieval in citrate buffer, pH 6.0 (Vector Laboratories H-3300-250) using a Decloaking Chamber (Biocare Medical). To block endogenous peroxidase activity, 3%

H_2O_2 (Fisher Scientific 7722-84-1) was used. And endogenous biotin was blocked by using the Avidin/Biotin Blocking kit (Vector Laboratories SP-2001). After incubation of primary antibodies (1:1000) overnight, the signal was developed by the R.T.U. Vectastain Kit (Vector PK-7100) and 3,3'-diaminobenzidine in chromogen solution (Agilent K3467). Hematoxylin (Agilent CS70030-2) then used to counterstain the nucleus. Antibodies used in IHC were CD3: Abcam #ab16669; CD4: Abcam #ab183685; CD8α: Cell Signaling #98941S; PD1: Abcam #ab214421; CTLA4: Abcam #ab237712; LAG3: Abcam #ab209238; TIGIT: Abcam #ab300073; TIM3: Abcam #ab2413332.

Anti-PD1 Antibody Treatment. The InVivoPlus anti-mouse PD1 (CD279) antibody was purchased from BioxCell (#BP0273). The PD1 antibody was diluted in InVivoPure pH7 Dilution buffer (BioxCell #IP0070) to make a 12.5 μg/mg (average of 22 mg mice) solution. After mice were implanted with p-αKO cells, 100μl of prepared mixture or the dilution buffer were injected intraperitoneally to mice weekly for 8 weeks. Mice were imaged by IVIS from week 5 to week 8, and mice survival data were recorded for survival studies.

Statistical Analysis. All statistical analyses were done by Graphpad Prism 9. For all statistical comparisons, 2-tailed Student's *t* test was used for comparison between 2 groups. The one-way ANOVA with Bonferroni's post hoc test and Kruskal-Wallis test with Dunn's post hoc test were used for multi-group comparisons. *p* values less than 0.05 were considered statistically significant.

Study Approval. All experiments in mice were conducted in accordance with the Office of Laboratory Animal Welfare and approved by the IACUC of Stony Brook University, Stony Brook, New York.

Data Availability. The scRNA-seq data and codes for data analysis are available upon request from the corresponding author.

AUTHOR CONTRIBUTIONS

H.V.H. conceived, designed and performed most the experiments and wrote the manuscript.

R.E. performed most of the bioinformatics analysis

B.R. prepared the tissue samples for single-cell sequencing

S.M. performed the metabolomics experiments

K.L. prepared the mouse GeCKO library and transfected the tumors cells for the genetic screen

Y.P.J. performed the mouse tumor implantation

W.Y.Z. analyzed the data and edited the manuscript

R.Z.L. conceived the study, analyzed the data and wrote the manuscript

ACKNOWLEDGMENTS

This study was supported in part by Department of Veterans Affairs Merit Review BX004083 and National Institute of Health R21CA274425 (R.Z.L.) and R01CA129536, R01CA236242, and R01CA224550 (W.X.Z.).

REFERENCES

1. Siegel RL, Miller KD, Wagle NS, Jemal A. Cancer statistics, 2023. *CA Cancer J Clin*. Jan 2023;73(1):17-48. doi:10.3322/caac.21763

2. Halbrook CJ, Lyssiotis CA, Pasca di Magliano M, Maitra A. Pancreatic cancer: Advances and challenges. *Cell*. Apr 13 2023;186(8):1729-1754. doi:10.1016/j.cell.2023.02.014

3. Moore AR, Rosenberg SC, McCormick F, Malek S. RAS-targeted therapies: is the undruggable drugged? *Nat Rev Drug Discov*. Aug 2020;19(8):533-552. doi:10.1038/s41573-020-0068-6

4. Wu CY, Carpenter ES, Takeuchi KK, et al. PI3K regulation of RAC1 is required for KRAS-induced pancreatic tumorigenesis in mice. *Gastroenterology*. Dec 2014;147(6):1405-16.e7. doi:10.1053/j.gastro.2014.08.032

5. Sivaram N, McLaughlin PA, Han HV, et al. Tumor-intrinsic PIK3CA represses tumor immunogenecity in a model of pancreatic cancer. *J Clin Invest*. May 21 2019;129(8):3264-3276. doi:10.1172/jci123540

6. Fan J-q, Wang M-F, Chen H-L, Shang D, Das JK, Song J. Current advances and outlooks in immunotherapy for pancreatic ductal adenocarcinoma. *Molecular Cancer*. 2020/02/15 2020;19(1):32. doi:10.1186/s12943-020-01151-3

7. Johnson BA, Yarchoan M, Lee V, Laheru DA, Jaffee EM. Strategies for Increasing Pancreatic Tumor Immunogenicity. *Clinical Cancer Research*. 2017;23(7):1656-1669. doi:10.1158/1078-0432.ccr-16-2318

8. Bian J, Almhanna K. Pancreatic cancer and immune checkpoint inhibitors-still a long way to go. *Transl Gastroenterol Hepatol*. 2021;6:6. doi:10.21037/tgh.2020.04.03

9. Liu L, Huang X, Shi F, et al. Combination therapy for pancreatic cancer: anti-PD-(L)1-based strategy. *J Exp Clin Cancer Res*. Feb 9 2022;41(1):56. doi:10.1186/s13046-022-02273-w

10. Li H-B, Yang Z-H, Guo Q-Q. Immune checkpoint inhibition for pancreatic ductal adenocarcinoma: limitations and prospects: a systematic review. *Cell Communication and Signaling*. 2021/11/24 2021;19(1):117. doi:10.1186/s12964-021-00789-w

11. Freed-Pastor WA, Lambert LJ, Ely ZA, et al. The CD155/TIGIT axis promotes and maintains immune evasion in neoantigen-expressing pancreatic cancer. *Cancer Cell*. Oct 11 2021;39(10):1342-1360.e14. doi:10.1016/j.ccell.2021.07.007

12. Gulhati P, Schalck A, Jiang S, et al. Targeting T cell checkpoints 41BB and LAG3 and myeloid cell CXCR1/CXCR2 results in antitumor immunity and durable response in pancreatic cancer. *Nature Cancer*. 2023/01/01 2023;4(1):62-80. doi:10.1038/s43018-022-00500-z

13. Panni RZ, Herndon JM, Zuo C, et al. Agonism of CD11b reprograms innate immunity to sensitize pancreatic cancer to immunotherapies. *Sci Transl Med*. Jul 3 2019;11(499)doi:10.1126/scitranslmed.aau9240

14. Vonderheide RH. CD40 Agonist Antibodies in Cancer Immunotherapy. *Annu Rev Med*. Jan 27 2020;71:47-58. doi:10.1146/annurev-med-062518-045435

15. Zhu Y, Herndon JM, Sojka DK, et al. Tissue-Resident Macrophages in Pancreatic Ductal Adenocarcinoma Originate from Embryonic Hematopoiesis and Promote Tumor Progression. *Immunity*. Aug 15 2017;47(2):323-338.e6. doi:10.1016/j.immuni.2017.07.014

16. Wu Y, Yi M, Niu M, Mei Q, Wu K. Myeloid-derived suppressor cells: an emerging target for anticancer immunotherapy. *Mol Cancer*. Sep 26 2022;21(1):184. doi:10.1186/s12943-022-01657-y

17. Baleeiro RB, Bouwens CJ, Liu P, et al. MHC class II molecules on pancreatic cancer cells indicate a potential for neo-antigen-based immunotherapy. *Oncoimmunology*. 2022;11(1):2080329. doi:10.1080/2162402x.2022.2080329

18. Yamamoto K, Venida A, Yano J, et al. Autophagy promotes immune evasion of pancreatic cancer by degrading MHC-I. *Nature*. 2020/05/01 2020;581(7806):100-105. doi:10.1038/s41586-020-2229-5

19. Hegde S, Krisnawan VE, Herzog BH, et al. Dendritic Cell Paucity Leads to Dysfunctional Immune Surveillance in Pancreatic Cancer. *Cancer Cell*. Mar 16 2020;37(3):289-307.e9. doi:10.1016/j.ccell.2020.02.008

20. Jiang H, Hegde S, Knolhoff BL, et al. Targeting focal adhesion kinase renders pancreatic cancers responsive to checkpoint immunotherapy. *Nat Med*. Aug 2016;22(8):851-60. doi:10.1038/nm.4123

21. Özdemir BC, Pentcheva-Hoang T, Carstens JL, et al. Depletion of carcinoma-associated fibroblasts and fibrosis induces immunosuppression and accelerates pancreas cancer with reduced survival. *Cancer Cell*. Jun 16 2014;25(6):719-34. doi:10.1016/j.ccr.2014.04.005

22. Shi C, Washington MK, Chaturvedi R, et al. Fibrogenesis in pancreatic cancer is a dynamic process regulated by macrophage-stellate cell interaction. *Lab Invest*. Apr 2014;94(4):409-21. doi:10.1038/labinvest.2014.10

23. Johnson BA, 3rd, Yarchoan M, Lee V, Laheru DA, Jaffee EM. Strategies for Increasing Pancreatic Tumor Immunogenicity. *Clin Cancer Res*. Apr 1 2017;23(7):1656-1669. doi:10.1158/1078-0432.Ccr-16-2318

24. Popovic A, Jaffee EM, Zaidi N. Emerging strategies for combination checkpoint modulators in cancer immunotherapy. *J Clin Invest*. Aug 1 2018;128(8):3209-3218. doi:10.1172/jci120775

25. Mace TA, Shakya R, Pitarresi JR, et al. IL-6 and PD-L1 antibody blockade combination therapy reduces tumour progression in murine models of pancreatic cancer. *Gut*. Feb 2018;67(2):320-332. doi:10.1136/gutjnl-2016-311585

26. Dey P, Li J, Zhang J, et al. Oncogenic KRAS-Driven Metabolic Reprogramming in Pancreatic Cancer Cells Utilizes Cytokines from the Tumor Microenvironment. *Cancer Discov*. Apr 2020;10(4):608-625. doi:10.1158/2159-8290.Cd-19-0297

27. Markham A. Alpelisib: First Global Approval. *Drugs*. Jul 2019;79(11):1249-1253. doi:10.1007/s40265-019-01161-6

28. Yang J, Nie J, Ma X, Wei Y, Peng Y, Wei X. Targeting PI3K in cancer: mechanisms and advances in clinical trials. *Molecular Cancer*. 2019;18(1)doi:10.1186/s12943-019-0954-x

29. Fazio N, Buzzoni R, Baudin E, et al. A Phase II Study of BEZ235 in Patients with Everolimus-resistant, Advanced Pancreatic Neuroendocrine Tumours. *Anticancer Res*. Feb 2016;36(2):713-9.

30. Salazar R, Garcia-Carbonero R, Libutti SK, et al. Phase II Study of BEZ235 versus Everolimus in Patients with Mammalian Target of Rapamycin Inhibitor-Naïve Advanced Pancreatic Neuroendocrine Tumors. *Oncologist*. Jul 2018;23(7):766-e90. doi:10.1634/theoncologist.2017-0144

31. Shapiro GI, Bell-McGuinn KM, Molina JR, et al. First-in-Human Study of PF-05212384 (PKI-587), a Small-Molecule, Intravenous, Dual Inhibitor of PI3K and mTOR in Patients with Advanced Cancer. *Clin Cancer Res*. Apr 15 2015;21(8):1888-95. doi:10.1158/1078-0432.Ccr-14-1306

32. Bedard PL, Tabernero J, Janku F, et al. A phase Ib dose-escalation study of the oral pan-PI3K inhibitor buparlisib (BKM120) in combination with the oral MEK1/2 inhibitor trametinib (GSK1120212) in patients with selected advanced solid tumors. *Clin Cancer Res*. Feb 15 2015;21(4):730-8. doi:10.1158/1078-0432.Ccr-14-1814

33. Ebrahimi S, Hosseini M, Shahidsales S, et al. Targeting the Akt/PI3K Signaling Pathway as a Potential Therapeutic Strategy for the Treatment of Pancreatic Cancer. *Curr Med Chem*. 2017;24(13):1321-1331. doi:10.2174/0929867324666170206142658

34. Wongkittichote P, Ah Mew N, Chapman KA. Propionyl-CoA carboxylase - A review. *Mol Genet Metab*. Dec 2017;122(4):145-152. doi:10.1016/j.ymgme.2017.10.002

35. Shchelochkov OA, Carrillo N, Venditti C. Propionic Acidemia. In: Adam MP, Everman DB, Mirzaa GM, et al, eds. *GeneReviews(®)*. University of Washington, Seattle
Copyright © 1993-2022, University of Washington, Seattle. GeneReviews is a registered trademark of the University of Washington, Seattle. All rights reserved.; 1993.

36. Grünert SC, Müllerleile S, De Silva L, et al. Propionic acidemia: clinical course and outcome in 55 pediatric and adolescent patients. *Orphanet J Rare Dis*. Jan 10 2013;8:6. doi:10.1186/1750-1172-8-6

37. Andreatta M, Corria-Osorio J, Müller S, Cubas R, Coukos G, Carmona SJ. Interpretation of T cell states from single-cell transcriptomics data using reference atlases. *Nature Communications*. 2021/05/20 2021;12(1):2965. doi:10.1038/s41467-021-23324-4

38. Tu AA, Gierahn TM, Monian B, et al. TCR sequencing paired with massively parallel 3′ RNA-seq reveals clonotypic T cell signatures. *Nature Immunology*. 2019;20(12):1692-1699. doi:10.1038/s41590-019-0544-5

39. Sun P, Zhang X, Wang R-J, et al. PI3Kα inhibitor CYH33 triggers antitumor immunity in murine breast cancer by activating CD8+T cells and promoting fatty acid metabolism. *Journal for ImmunoTherapy of Cancer*. 2021;9(8):e003093. doi:10.1136/jitc-2021-003093

40. Peng W, Chen JQ, Liu C, et al. Loss of PTEN Promotes Resistance to T Cell-Mediated Immunotherapy. *Cancer Discov*. Feb 2016;6(2):202-16. doi:10.1158/2159-8290.Cd-15-0283

41. Liu Y-T, Sun Z-J. Turning cold tumors into hot tumors by improving T-cell infiltration. *Theranostics*. 2021;11(11):5365-5386. doi:10.7150/thno.58390

42. Borcoman E, De La Rochere P, Richer W, et al. Inhibition of PI3K pathway increases immune infiltrate in muscle-invasive bladder cancer. *Oncoimmunology*. 2019;8(5):e1581556. doi:10.1080/2162402x.2019.1581556

43. Sai J, Owens P, Novitskiy SV, et al. PI3K Inhibition Reduces Mammary Tumor Growth and Facilitates Antitumor Immunity and Anti-PD1 Responses. *Clin Cancer Res*. Jul 1 2017;23(13):3371-3384. doi:10.1158/1078-0432.Ccr-16-2142

44. Sun P, Meng L-H. Emerging roles of class I PI3K inhibitors in modulating tumor microenvironment and immunity. *Acta Pharmacologica Sinica*. 2020;41(11):1395-1402. doi:10.1038/s41401-020-00500-8

45. Isoyama S, Mori S, Sugiyama D, et al. Cancer immunotherapy with PI3K and PD-1 dual-blockade via optimal modulation of T cell activation signal. *J Immunother Cancer*. Aug 2021;9(8)doi:10.1136/jitc-2020-002279

46. Collins NB, Al Abosy R, Miller BC, et al. PI3K activation allows immune evasion by promoting an inhibitory myeloid tumor microenvironment. *Journal for ImmunoTherapy of Cancer*. 2022;10(3):e003402. doi:10.1136/jitc-2021-003402

47. Kurczynski TW, Hoppel CL, Goldblatt PJ, Gunning WT. Metabolic studies of carnitine in a child with propionic acidemia. *Pediatr Res*. Jul 1989;26(1):63-6. doi:10.1203/00006450-198907000-00018

48. Ando T, Rasmussen K, Wright JM, Nyhan WL. Isolation and identification of methylcitrate, a major metabolic product of propionate in patients with propionic acidemia. *J Biol Chem*. Apr 10 1972;247(7):2200-4.

49. Smith PM, Howitt MR, Panikov N, et al. The microbial metabolites, short-chain fatty acids, regulate colonic Treg cell homeostasis. *Science*. Aug 2 2013;341(6145):569-73. doi:10.1126/science.1241165

50. Tedelind S, Westberg F, Kjerrulf M, Vidal A. Anti-inflammatory properties of the short-chain fatty acids acetate and propionate: a study with relevance to inflammatory bowel disease. *World J Gastroenterol*. May 28 2007;13(20):2826-32. doi:10.3748/wjg.v13.i20.2826

51. Høgh RI, Møller SH, Jepsen SD, et al. Metabolism of short-chain fatty acid propionate induces surface expression of NKG2D ligands on cancer cells. *The FASEB Journal*. 2020;34(11):15531-15546. doi:10.1096/fj.202000162r

52. Chauvin J-M, Zarour HM. TIGIT in cancer immunotherapy. *Journal for ImmunoTherapy of Cancer*. 2020;8(2):e000957. doi:10.1136/jitc-2020-000957

53. Ge Z, Peppelenbosch MP, Sprengers D, Kwekkeboom J. TIGIT, the Next Step Towards Successful Combination Immune Checkpoint Therapy in Cancer. *Front Immunol*. 2021;12:699895. doi:10.3389/fimmu.2021.699895

54. Peng H, Li L, Zuo C, et al. Combination TIGIT/PD-1 blockade enhances the efficacy of neoantigen vaccines in a model of pancreatic cancer. *Front Immunol*. 2022;13:1039226. doi:10.3389/fimmu.2022.1039226

55. Wang Y, Kuramitsu Y, Baron B, et al. PI3K inhibitor LY294002, as opposed to wortmannin, enhances AKT phosphorylation in gemcitabine-resistant pancreatic cancer cells. *Int J Oncol*. Feb 2017;50(2):606-612. doi:10.3892/ijo.2016.3804

56. Gharbi SI, Zvelebil MJ, Shuttleworth SJ, et al. Exploring the specificity of the PI3K family inhibitor LY294002. *Biochem J*. May 15 2007;404(1):15-21. doi:10.1042/bj20061489

57. Miller MS, Thompson PE, Gabelli SB. Structural Determinants of Isoform Selectivity in PI3K Inhibitors. *Biomolecules*. Feb 26 2019;9(3)doi:10.3390/biom9030082

58. Kong D, Yamori T. Phosphatidylinositol 3-kinase inhibitors: promising drug candidates for cancer therapy. *Cancer Sci*. Sep 2008;99(9):1734-40. doi:10.1111/j.1349-7006.2008.00891.x

59. Chen S, Sanjana NE, Zheng K, et al. Genome-wide CRISPR screen in a mouse model of tumor growth and metastasis. *Cell*. Mar 12 2015;160(6):1246-60. doi:10.1016/j.cell.2015.02.038

60. Joung J, Konermann S, Gootenberg JS, et al. Genome-scale CRISPR-Cas9 knockout and transcriptional activation screening. *Nature Protocols*. 2017;12(4):828-863. doi:10.1038/nprot.2017.016

FIGURE LEGEND

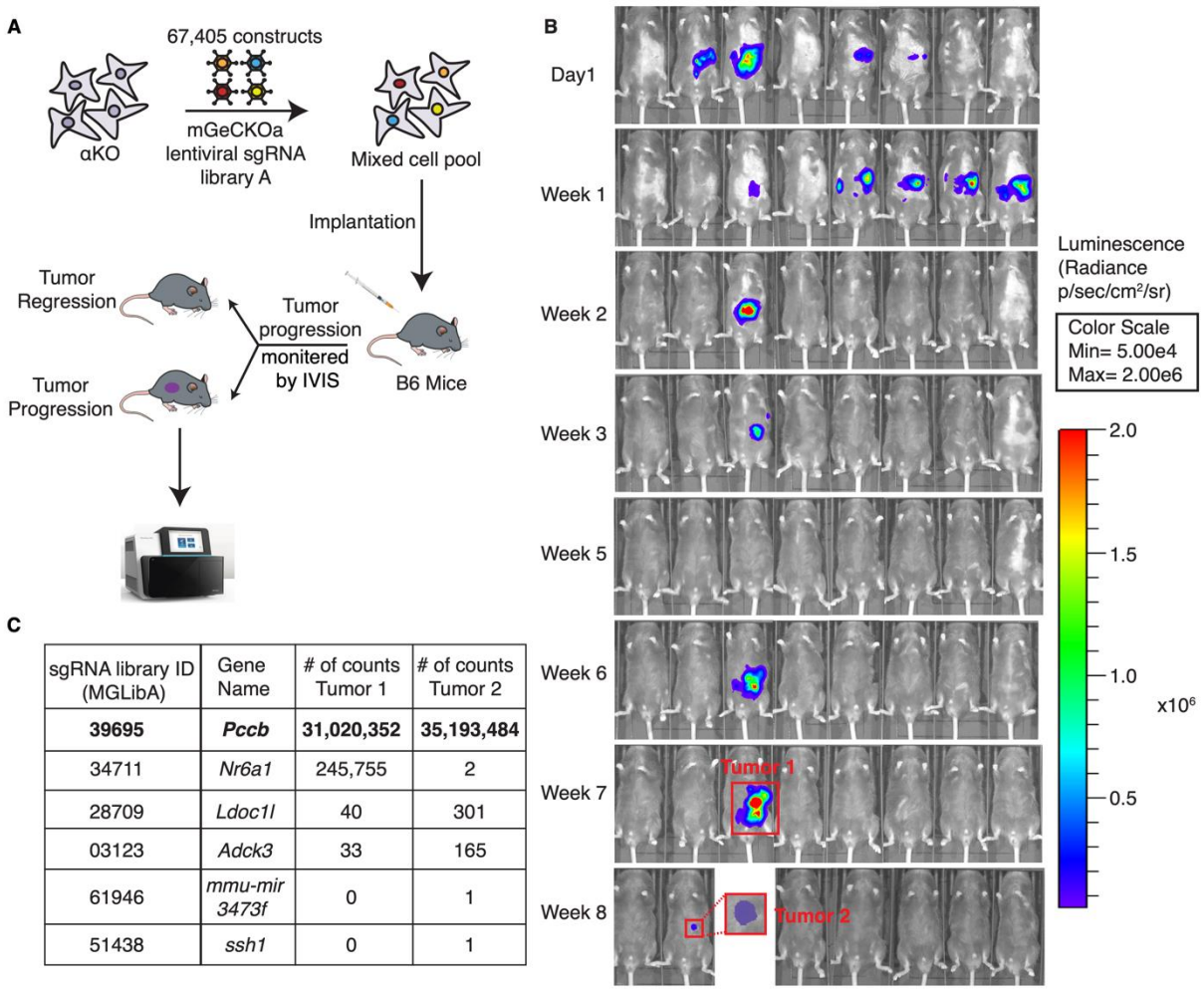

C

sgRNA library ID (MGLibA)	Gene Name	# of counts Tumor 1	# of counts Tumor 2
39695	***Pccb***	**31,020,352**	**35,193,484**
34711	*Nr6a1*	245,755	2
28709	*Ldoc1l*	40	301
03123	*Adck3*	33	165
61946	*mmu-mir 3473f*	0	1
51438	*ssh1*	0	1

Figure 1. Genome-wide CRISPR gene-deletion screen identifies *Pccb* contributing to PIK3CA-mediated pancreatic tumor immune evasion. (A) A schema for screen. Mouse genome-scale CRISPR/Cas9 knockout library (mGeCKO v2A) containing three sgRNA each for 20611 genes was transduced into *Kras*$^{G12D/+}$;*Tp53*$^{R172H/+}$;*Pik3ca*$^{-/-}$ (αKO) cells. Pooled cells were implanted in the pancreas of eight C57BL/6J mice. **(B)** IVIS imaging was performed to monitor tumor progression in these mice. In two animals, tumors were still present at the end of the screen (annotated as tumor 1 & 2). **(C)** Harvested DNAs prepared from the tumors were subjected to next generation sequencing (NGS) to identify enriched sgRNAs barcodes. Sequences corresponding to only six genes in the mGeCKO v2A library have detectable NGS counts as shown in the table. In both tumors, sgRNA sequences mapping to the *Pccb* gene are most numerous.

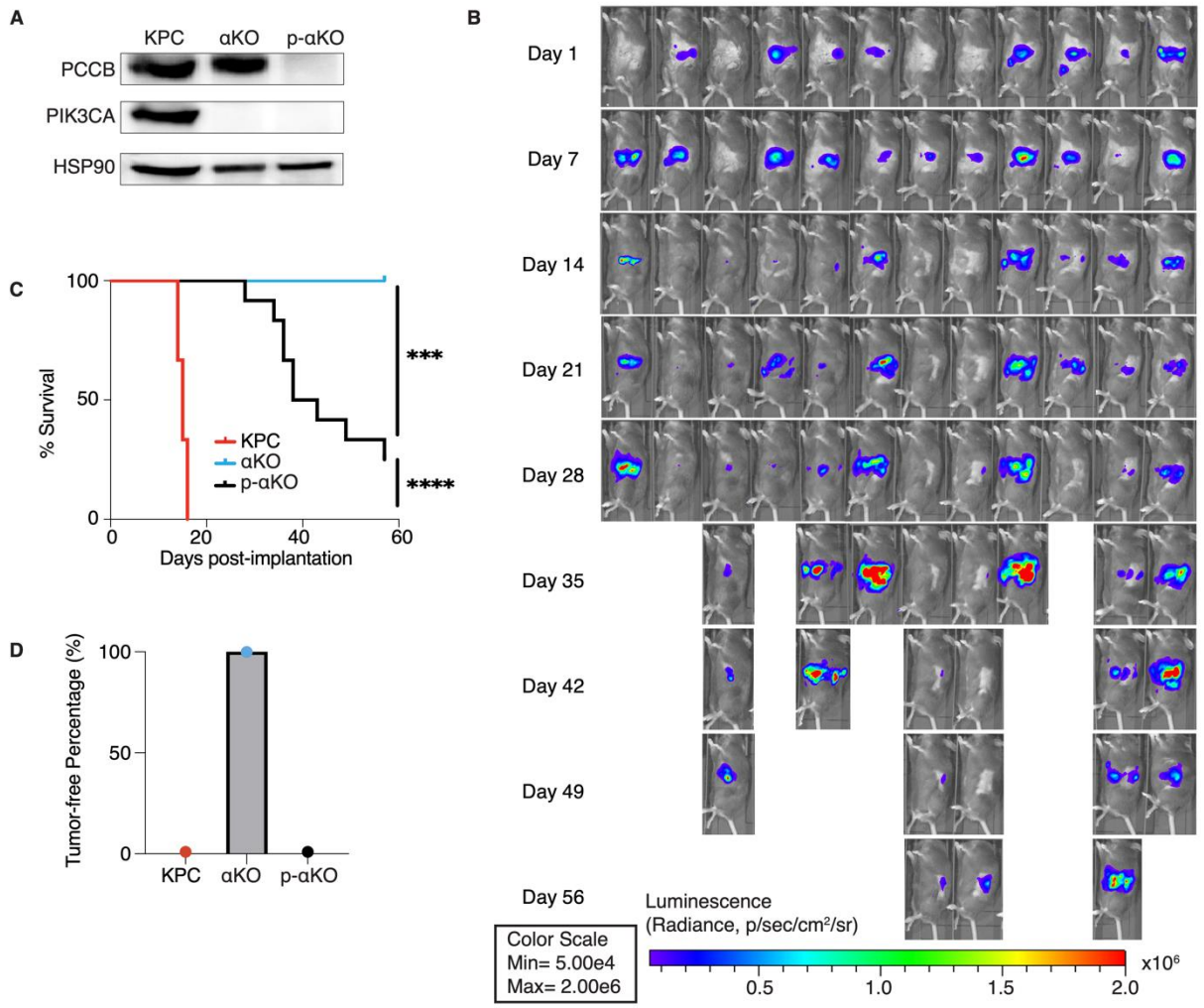

Figure 2. *Pccb* deletion in *Kras$^{G12D/+}$;Tp53$^{R172H/+}$;Pik3ca$^{-/-}$* (αKO) *cells* reverses the immune-surveillance phenotype. (A) *Pccb* was deleted in αKO cells by CRISPR/Cas9 to generate p-αKO cells. Western blotting confirmed PCCB and PIK3CA loss in p-αKO cells. **(B)** Orthotopic implantation of p-αKO tumors in the pancreas of C57BL/6J mice was monitored by IVIS imaging of the luciferase signal weekly for 8 weeks. **(C)** Kaplan-Meier survival curves for mice implanted with KPC, αKO, and p-αKO cells. Median survival KPC: 15.5 days (N=8); αKO, all alive (N=9); p-αKO, 40.5 days (N=12). ****P < 0.0001 for KPC vs. αKO; ***P=0.0009 for αKO vs. p-αKO; ****P < 0.0001 for KPC vs. p-αKO (log-rank test). **(D)** Tumor free survival percentage for KPC (0%), αKO (100%) and p-αKO (0%) implanted to B6 mice for 8 weeks.

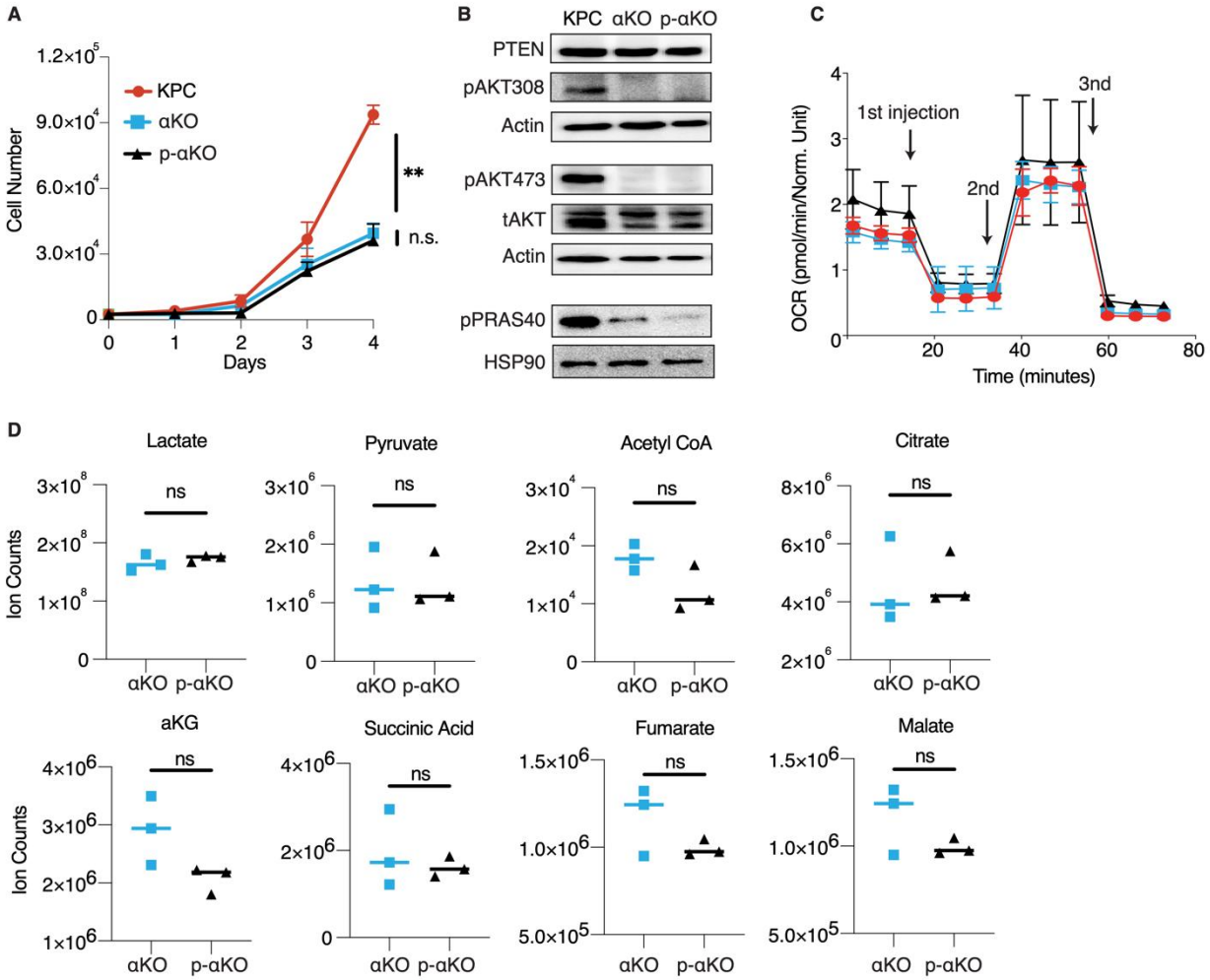

Figure 3. *In vitro* characterization of *Kras$^{G12D/+}$;Tp53$^{R172H/+}$;Pik3ca$^{-/-}$;Pccb$^{-/-}$* (p-αKO) cells. **(A)** Growth rates of KPC, αKO and p-αKO cell lines in culture were measured from day 1 to day 4 (mean ± SD, n=3). ***P= 0.0009 for KPC vs. p-αKO; not significant (ns) for αKO vs. p-αKO (One-way ANOVA). **(B)** Western blotting of PTEN, phospho-Thr308 AKT, phospho-Ser473 AKT, and phospho-PRAS40. Actin and HSP90 were used as loading controls. **(C)** Mitochondria function was evaluated by measuring the oxygen consumption rate (OCR) with Seahorse. 1st injection: oligomycin; 2nd injection: FCCP; 3rd injection: antimycin A & rotenone. **(D)** LC-MS exploring changes of metabolites of the TCA cycle. Data are represented as ion counts ± SD (N=3 for all groups). ns: not significant.

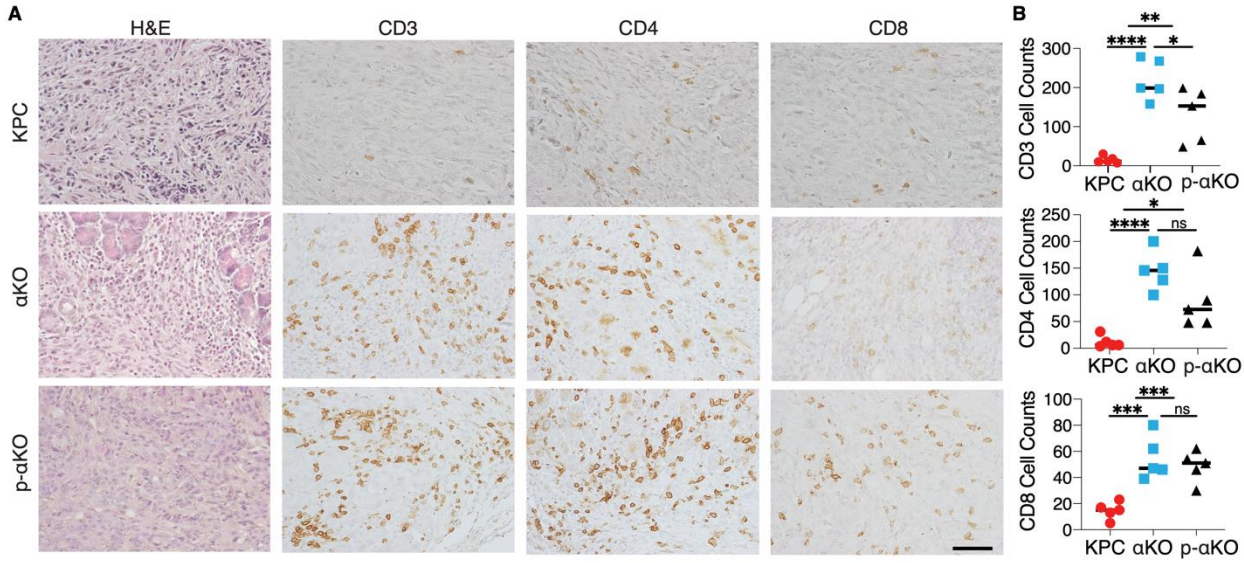

Figure 4. The presence of infiltrating T cells in *Kras$^{G12D/+}$;Tp53$^{R172H/+}$;Pik3ca$^{-/-}$;Pccb$^{-/-}$* (p-αKO) tumors. (A) Pancreatic tissue sections prepared from C57BL/6J mice implanted with KPC, αKO, and p-αKO cells. Tumor sections were stained with H&E and IHC with CD3, CD4, and CD8 antibodies. Representative sections are shown. Scale bar: 60μm. **(B)** Quantification of tumor-infiltrating T cells in 5 representative tumor sections for each group (mean ± SD, n=3). CD3: ****P<0.0001 for KPC vs. αKO; **P=0.0063 for KPC vs. p-αKO; *P=0.0471 for αKO vs. p-αKO. CD4: ****P<0.0001 for KPC vs. αKO; *P=0.0164 for KPC vs. p-αKO; ns for αKO vs. p-αKO. CD8: ***P=0.0009 for KPC vs. αKO; ***P=0.0005 for KPC vs. p-αKO; and ns for αKO vs. p-αKO (two-tailed t test). ns: not significant.

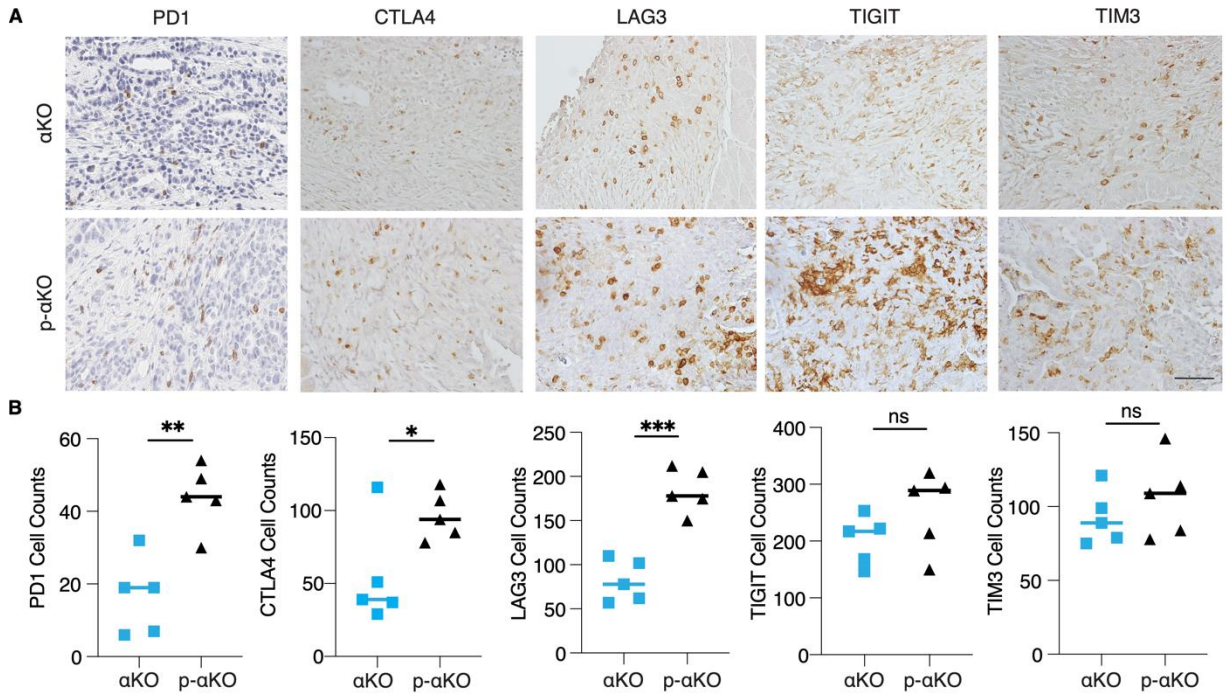

Figure 5. Expression of T cell checkpoint markers in αKO and p-αKO tumors. (A) αKO and p-αKO cells were implanted into the pancreas of C57BL/6J mice. Tumor sections were stained with checkpoint markers: PD1, CTLA4, LAG3, TIGIT and TIM3. Representative sections are shown. Scale bars: 60 μm. **(B)** Quantifications of cells positive for each checkpoint marker at representative tumor sections (mean ± SD, N=5). αKO vs. p-αKO: **P = 0.0023 for PD1; *P = 0.0371 for CTLA4; ***P = 0.0002 for LAG3; ns for TIGIT and TIM3.

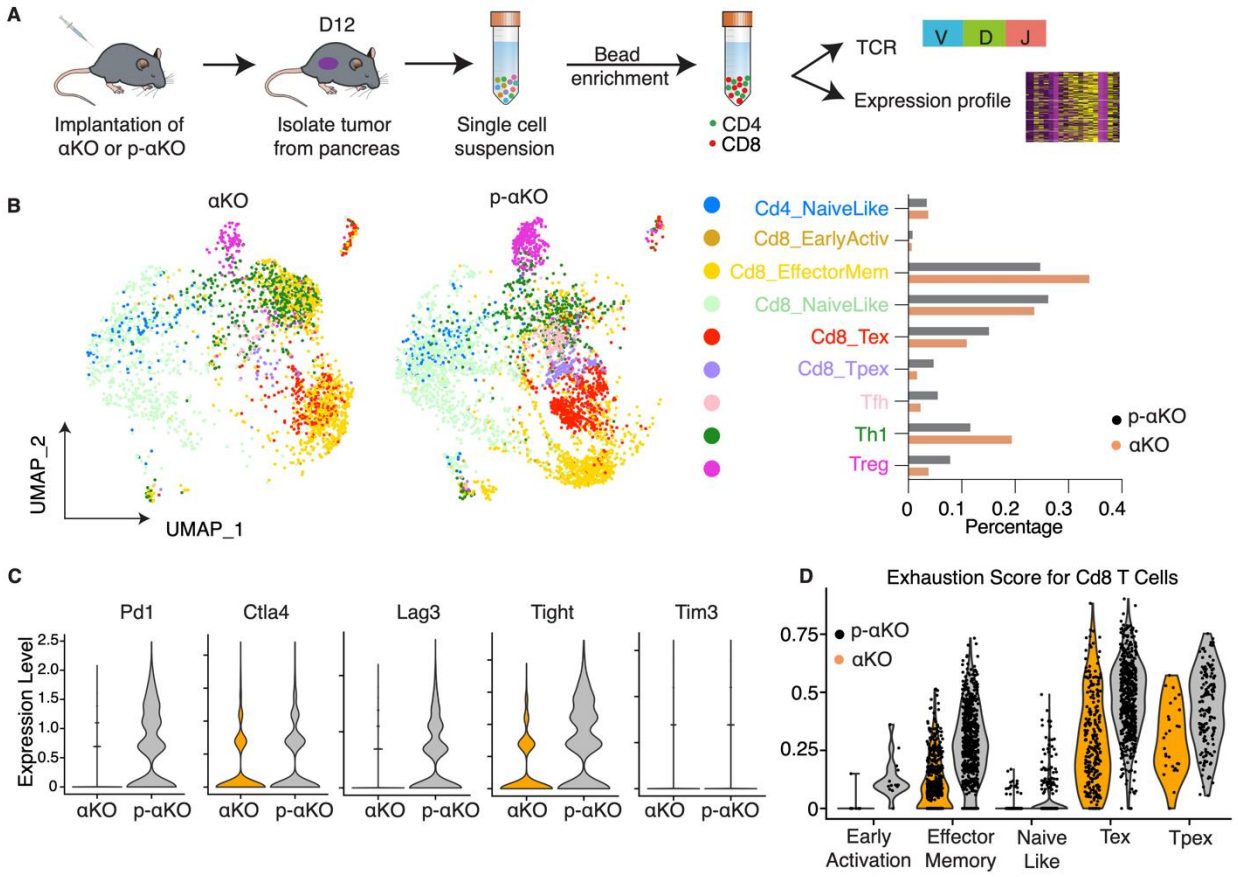

Figure 6. CD8⁺ infiltrating T cells in *Kras$^{G12D/+}$;Tp53$^{R172H/+}$;Pik3ca$^{-/-}$;Pccb$^{-/-}$* (p-αKO) tumors exhibit an "exhausted" gene-expression profile. (A) Experimental design schema for single cell RNA sequencing of infiltrating T cells in p-αKO vs. αKO tumors. Cells were implanted in the pancreas of C57BL/6J mice and tumors were harvested at 12 days post-implantation. Single cell suspensions were enriched with CD4⁺ and CD8⁺ beads followed by concurrent single-cell transcriptional and T-cell receptor (TCR) profiling using 10x Genomics protocols. **(B)** UMAP of infiltrating CD4⁺ and CD8⁺ T cells in αKO and p-αKO tumors. Principle component analysis of gene expression profiles generated 9 cell clusters annotated based by ProjectTILs. Cd8_EarlyActiv: early activated Cd8; Cd8_EffectorMem: effector memory Cd8; Cd8_Tex: exhausted Cd8; Cd8_Tpex: precursor exhausted Cd8; Tfh: follicular helper T cells; Th1: T helper type 1; Treg: regulatory T cells. Each dot corresponds to a single cell. **(C)** mRNA levels of Pdcd1, Ctla4, Lag3, Tigit, and Tim3 for Cd8+ T cells measured by scRNAseq. **(D)** T exhaustion scores calculated by SignatuR that includes 5 checkpoint markers (Pdcd1, Lag3, Ctla4, Tim3, and Tigit).

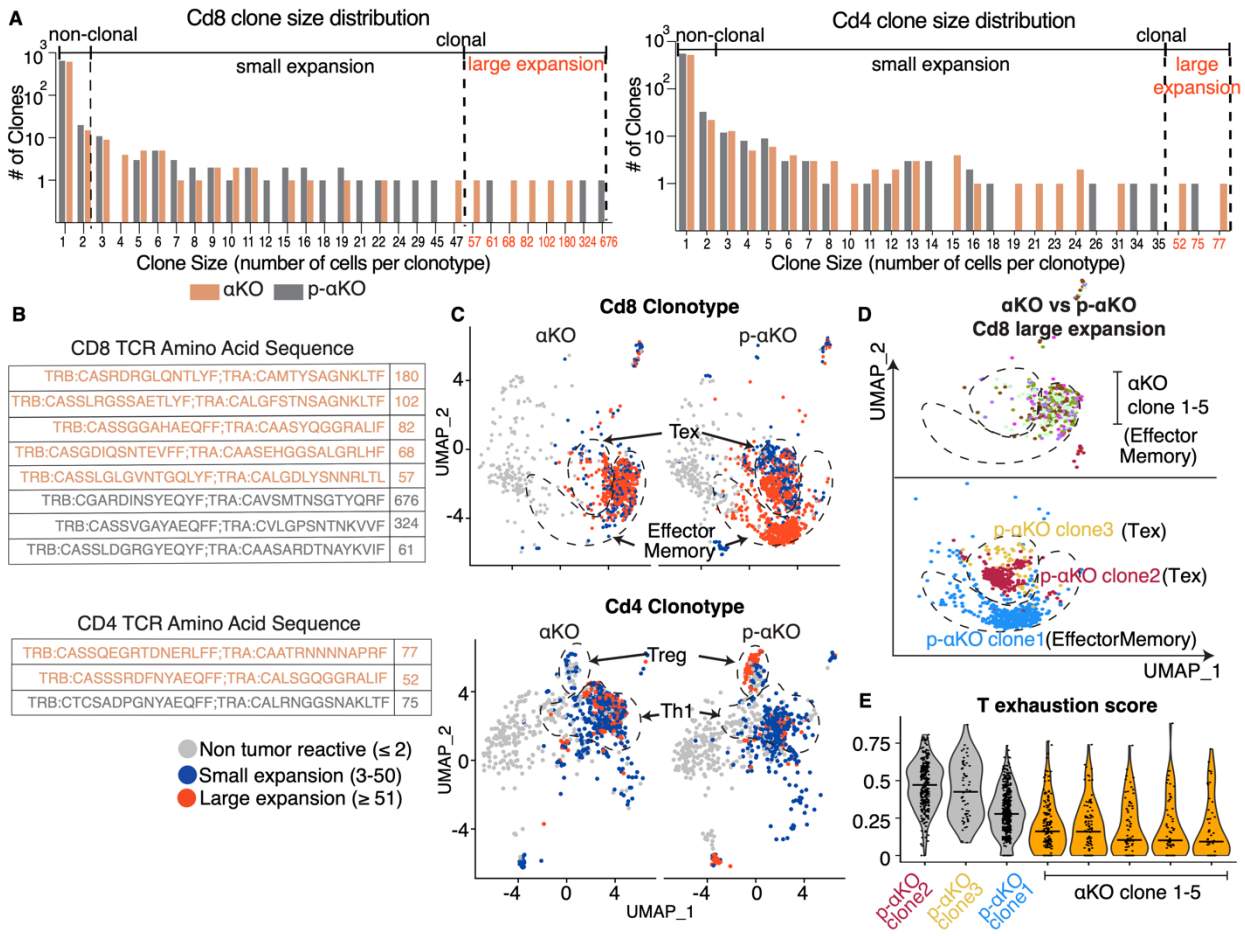

Figure 7. CD8⁺ T cell clones found in *Kras$^{G12D/+}$;Tp53$^{R172H/+}$;Pik3ca$^{-/-}$;Pccb$^{-/-}$* (p-αKO) tumors exhibit an "exhausted" gene-expression profile. (A) Size distribution for Cd8 and Cd4 T clonal types in αKO and p-αKO tumors. Non-clonal: N ≤ 2; small expansion: 3 ≤ N ≤ 50; large expansion: N ≥ 51. **(B)** Large expansions of Cd8 and Cd4 clones in each sample and their amino acid sequences of the CDR3 region are shown in the table. **(C)** Clonotype distribution of Cd4 and Cd8 in αKO and p-αKO tumors vary by clone sizes. Grey dots indicate T singlets and doublets (N ≤ 2); blue dots indicate small size clones (3 ≤ N ≤ 50); red dots indicate large size clones (N ≥ 51). The dashed regions are Cd8_EffectorMemory, Cd8_Tex, Treg, and Th1 groups. **(D)** The distribution of large size clones of Cd8 (N ≥ 51) in αKO and p-αKO tumors. αKO has 5 large size clones mapped to Cd8 effector memory group (labeled with dashed regions), p-αKO has 3 large size clones mapped to Cd8 effector memory and Tex groups (labeled with dashed regions). **(E)** T exhaustion scores calculated by SignatuR that includes 5 checkpoint markers (Pdcd1, Lag3, Ctla4, Tim3, and Tigit) for the large size clones in αKO (n=5) and p-αKO (n=3) tumors.

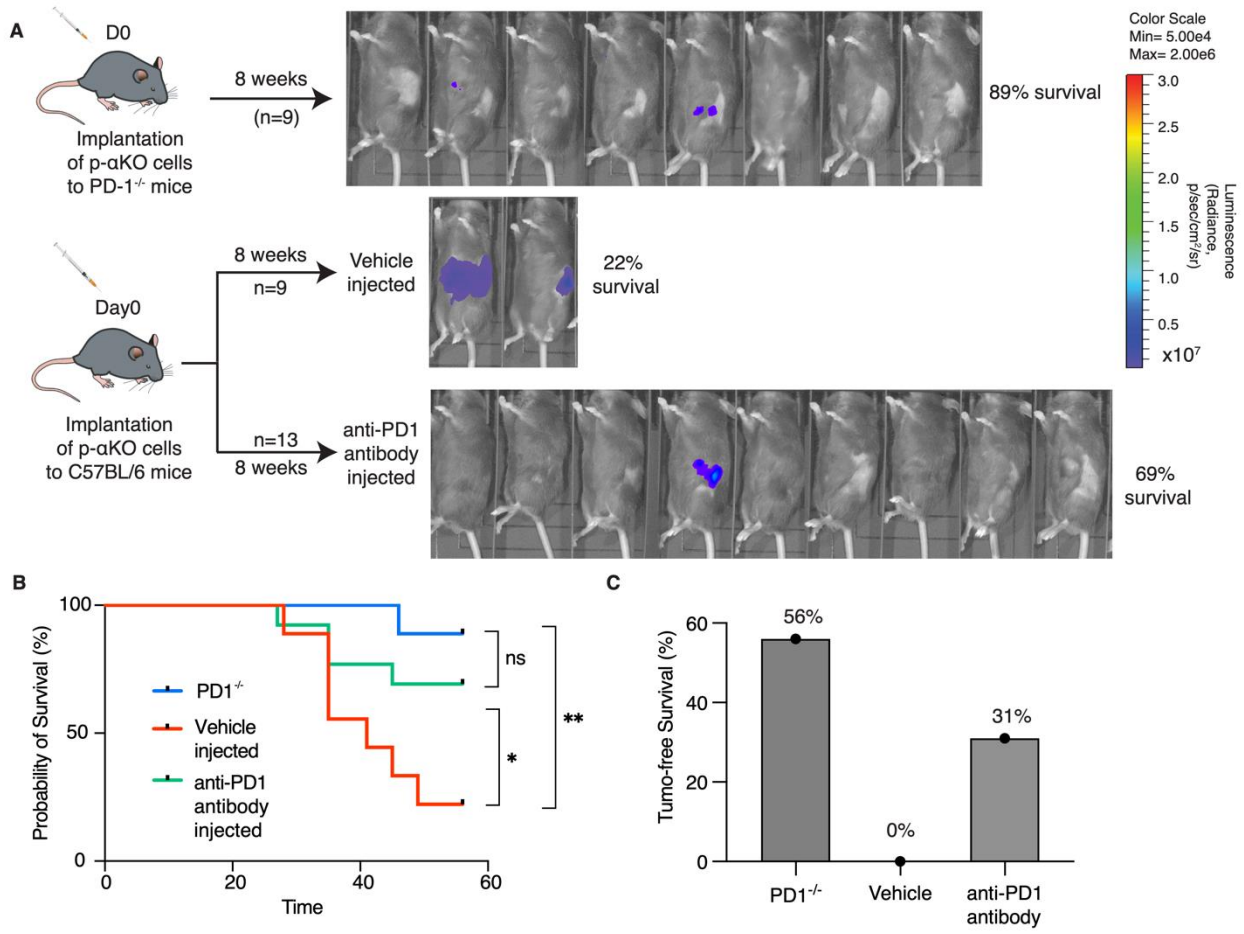

Figure 8. Treatment with a neutralizing anti-PD1 antibody attenuates p-αKO tumor progression and increases host animal survival. (A) PD1$^{-/-}$ mice (N = 9) were implanted with p-αKO cells in the pancreas and was monitored for 8 weeks. IVIS imaging was performed to assess tumor size at the end of the experiment. C57BL/6J mice (N = 22) were implanted with p-αKO cells in the pancreas and randomly divided into two groups. One group was injected with 12.5 mg/mg of PD1 neutralizing antibody weekly for 8 weeks, and the vehicle group was injected with the inVivo Pure dilution buffer. IVIS imaging was performed to assess tumor size at the end of the experiment. **(B)** Kaplan-Meier survival curves for PD1$^{-/-}$ mice implanted with p-αKO cells, and vehicle and anti-PD1 treated C57BL/6J mice implanted with p-αKO cells. Survival rate for PD1$^{-/-}$ group: 89%, median survival undefined; survival rate for vehicle injected group: 22%, median survival is 41 days; survival rate for anti-PD1 injected group: 69%, median survival undefined. *P = 0.0436 for vehicle vs. anti-PD1 antibody injection. **(C)** Tumor free survival percentage of PD1$^{-/-}$ (56%), vehicle (0%), and anti-PD1 antibody injected group (31%).

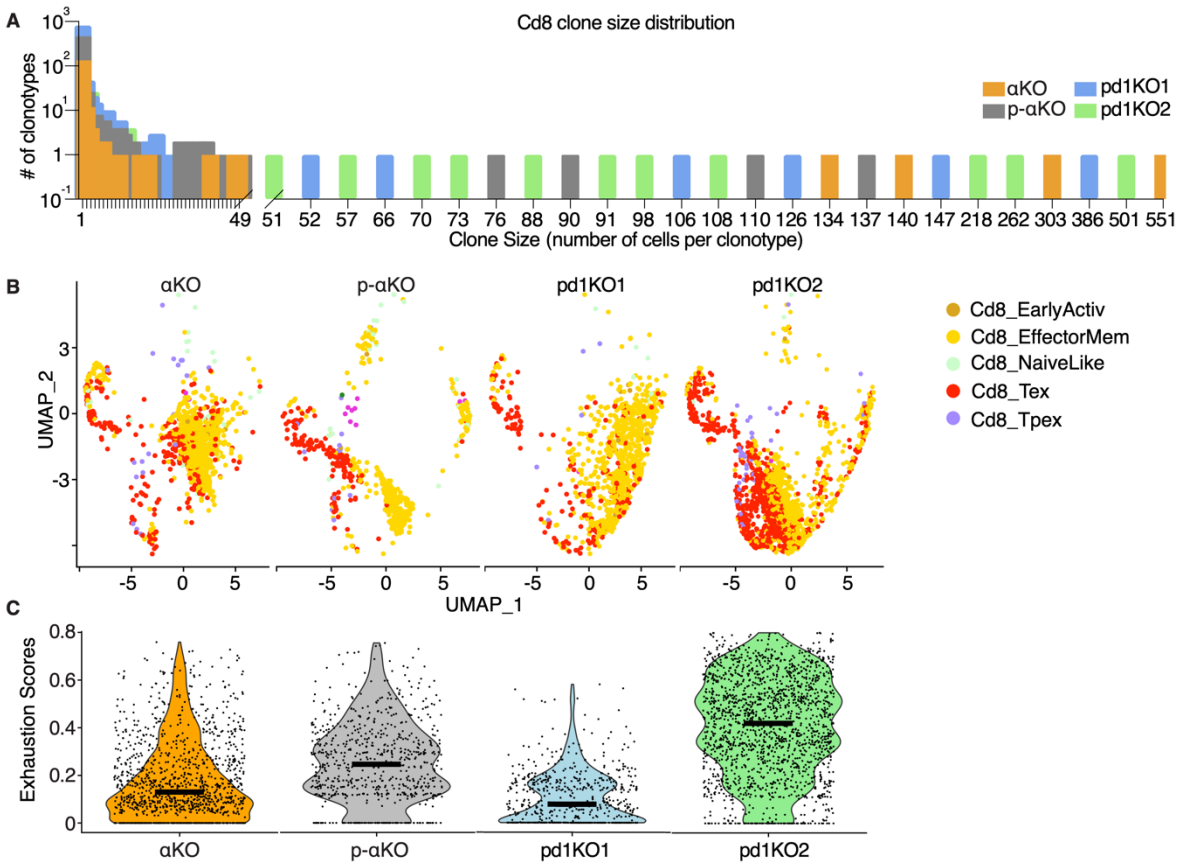

Figure 9. CD8 T cell clones from PD1KO1 and PD1KO2 exhibit reversal of the previously observed "exhausted phenotype". (A) Bar graph showing CD8 clone size distribution in αKO, p-αKO, PD1KO1, and PD1KO2 samples, with a significant proportion of clones exceeding size 50 observed in all samples. **(B)** The distribution of clones with size over 50 mapped to gene expression profiles in αKO, p-αKO, PD1KO1, and PD1KO2 samples. **(C)** Comparison of exhaustion scores for clone size exceeding 50 in all samples. T exhaustion scores calculated by SignatuR that includes 5 checkpoint markers (Pdcd1, Lag3, Ctla4, Tim3, and Tigit). Black line indicates the median scores.

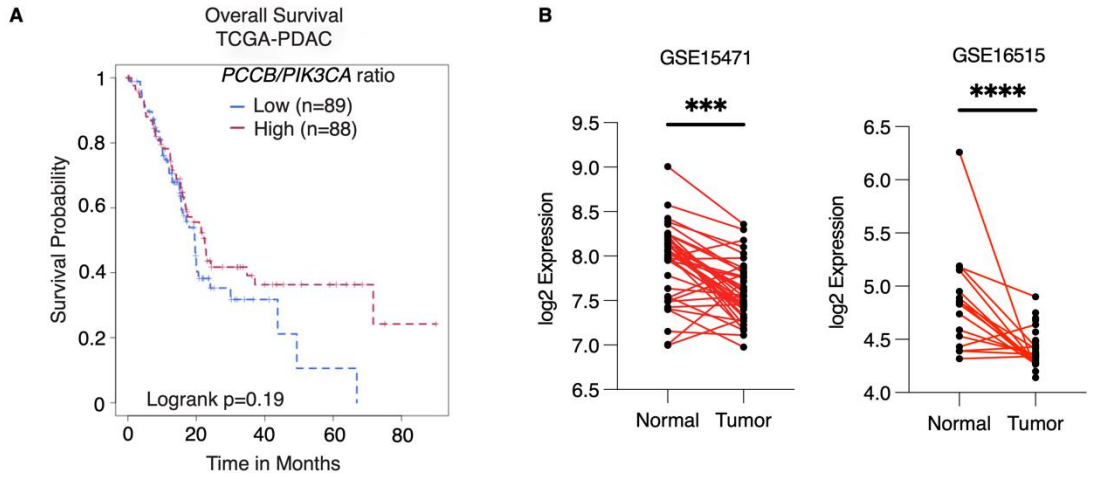

Figure 10. PCCB in PDAC patients. (A) Overall survival between patients with high *PCCB/PIK3CA* ratio vs. patients with low *PCCB/PIK3CA* of 177 PDAC patients from TCGA database. P=0.19. **(B)** Two PDAC clinical data GSE15471 and GSE16515 illustrating *PCCB* mRNA expression in tumor sections vs. adjacent normal tissues. ***P=0.0001 for GSE15471, N=36 for tumor, and N=36 for normal; and ****P<0.0001 for GSE16515, n=36 for tumor, and N=16 for normal.

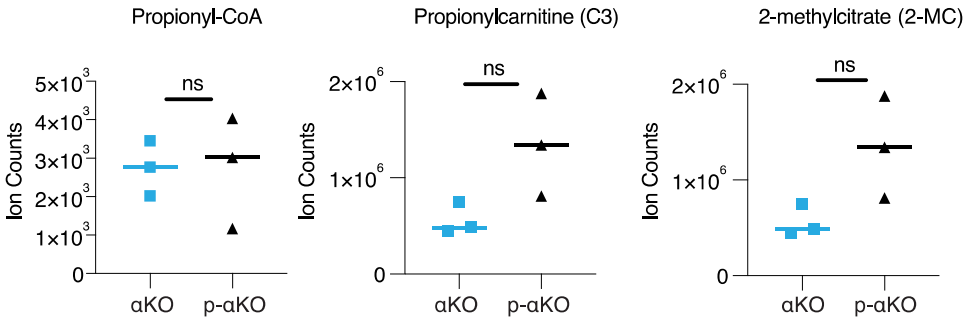

Supplemental Figure 1. LC-MS exploring changes of propionyl-CoA, propionylcarnitine, and 2-methylcitrate. Data are represented as ion counts ± SD (N=3 for all groups). ns: not significant.